Ocean Engineering 269 (2023) 113532

Contents lists available at ScienceDirect

Ocean Engineering

journal homepage: www.elsevier.com/locate/oceaneng

Dynamic mode decomposition and reconstruction of the transient propeller wake under a light loading condition

Yuchang Zhi [a], Rundi Qiu [b,c], Renfang Huang [b,*], Yiwei Wang [b,c,d]

[a] School of Aeronautics and Astronautics, Sun Yat-Sen University, Guangzhou, 510275, China
[b] Key Laboratory for Mechanics in Fluid Solid Coupling Systems, Institute of Mechanics, Chinese Academy of Sciences, Beijing, 100190, China
[c] School of Future Technology, University of Chinese Academy of Sciences, Beijing, 100049, China
[d] School of Engineering Science, University of Chinese Academy of Sciences, Beijing, 100049, China

ARTICLE INFO

Handling Editor: Prof. A.I. Incecik

Keywords:
E779A propeller
Propeller wake
Dynamic mode decomposition
Reconstruction
LES

ABSTRACT

This research aims to extend our understanding of propeller wake dynamics under a light loading condition, thereby laying a foundation for design optimization and flow control of the propeller. Dynamic mode decomposition (DMD) and reconstruction are used to analyze the transient vortical wake structures obtained by large eddy simulation. The propeller wake includes stable tip and hub vortices without interacting evolution at the light loading condition, and elliptical instabilities are observed downstream of the tip vortices. DMD describes the most energetic modes and the corresponding dominant frequencies are the blade passing frequency and its multiples. The coherent structures identified via DMD are primarily associated with the ordered convection of the tip vortices and have little correlation with the hub vortices. Additionally, the propeller wake flow is reconstructed using the first four DMD modes, and the primary wake features are well restored with a maximum reconstructed error of 7.98%. This demonstrates that the flow-field reconstruction based on the DMD reduced-order model is promising for predicting the propeller wake and controlling the propeller operation.

1. Introduction

The propeller is a means of propulsion widely used in trans-media vehicles. When the propeller is running at high speed, a sophisticated wake field is formed, including blade trailing edge vortices (Felli et al., 2011), tip vortices (Wang et al., 2021a), and a hub vortex (Heydari and Sadat-Hosseini, 2020). Up to now, much effort has been made to investigate propeller wake behaviors, such as elliptical instability (Blanco-Rodríguez and Le Dizès, 2016), breakdown (Hattori and Fukumoto, 2009), leap-frogging, meandering (Quaranta et al., 2015, 2019), and merging of tip vortices (Shi et al., 2022). However, the evolutionary mechanisms underlying the turbulent vortex structures in the propeller wake are still not comprehensively understood (Dubbioso et al., 2013; Felli and Falchi, 2018; Felli et al., 2008; Posa et al., 2019). The wake instabilities directly affect the propulsion efficiency and even increase the fatigue load, vibration, and noise of the propeller(Bai et al., 2022; Wu et al., 2018), thereby causing structural damage to ships or vehicles (Dubbioso and Ortolani, 2020; Guo et al., 2021; Heydari and Sadat-Hosseini, 2020; Kao and Lin, 2020; Posa et al., 2022). In-depth understanding of propeller wake characteristics is critical for design optimization and development of the next-generation propeller.

Experimental measurement is one of the most effective methods for studying the propeller wake. In the propeller wake experiments, the dynamic characteristics of complex vortex systems are usually captured by high-speed cameras (Felli et al., 2011), which can see the evolution of the vortex system in space and time. The velocity distribution of the propeller wake field is obtained by particle image velocimetry (PIV) technology (Di Felice, 2004; Felli and Felice, 2005; Felli et al., 2009; Paik et al., 2007). Felli et al. carried out experiments under different operating conditions to investigate the wake dynamics past an INSEAN E779A propeller by using the PIV technique together with pressure and velocity phase measurements (Felli et al., 2006). Their experiments focused on the effects of blade numbers (Felli et al., 2008), advance coefficients (Felli et al., 2011), and the oblique flow (Felli and Falchi, 2018) on the propeller vortex evolution, instability, and breakdown. The experimental results show that the propeller wake instability is related to the mutual inductance between adjacent helicoidal vortices (Felli et al., 2011), and the interaction between the tip vortices and hub vortex (Felli and Falchi, 2018). Lee (2002) used the particle image velocimetry (PIV) technique to measure the velocity distribution of a five-blade

* Corresponding author.
E-mail address: hrenfang@imech.ac.cn (R. Huang).

https://doi.org/10.1016/j.oceaneng.2022.113532
Received 1 June 2022; Received in revised form 10 December 2022; Accepted 22 December 2022
Available online 9 January 2023

propeller wake field and analyzed the statistical characteristics of the phase-averaged flow field. Paik et al. (2007) measured the wake characteristics of a four-blade propeller at a high Reynolds number via a double-frame PIV technique, and the phase-averaged velocity indicates that trailing edge vortices are related to radial velocity jump, and the wake is influenced by blade boundary layers and centrifugal forces. Cotroni et al. (2000) used a multigrid adaptive cross-correlation algorithm to the process the PIV images and obtained the high-resolution wake field past a four-blade propeller, revealing the contribution of the viscous wake generated by the blade boundary layer at various angular positions.

Due to the limitations of experimental techniques, many three-dimensional multi-scale vortex structures of the propeller wake cannot be directly measured. In contrast, computational fluid dynamics (CFD) is a very promising method that can more intuitively study the spatio-temporal evolution mechanisms of the propeller wake (Gong et al., 2021; Han et al., 2021; Li et al., 2021; Long et al., 2021; Posa et al., 2020; Qin et al., 2021; Wang et al., 2022a). Wang et al. (2021b, 2021c) simulated the wake dynamics for a propeller under different advance coefficients, and the calculated wake structures were consistent with the experiments. The vortex structure, kinetic energy power spectral density, and velocity distribution indicate that the tip vortex instability is related to the interaction of different vortex structures in the wake field, such as the mutual induction of tip vortices(Wang et al., 2021b). Ahmed et al. (2020) numerically studied the propeller wake characteristics at various advance coefficients using large eddy simulation (LES), and the simulated results were consistent with the experiments. They found that the mutual inductance between adjacent vortex sheets caused short-wave instabilities, the breakup of tip vortices, and long-wave instabilities. Muscari et al. (2013) used the Reynolds-averaged Navier–-Stokes (RANS) and the detached eddy simulation (DES) methods to simulate the vortex dynamics in the propeller wake and found that the RANS method could predict the global quantities but it is too dissipative to capture the unsteady fluctuations and the wake instabilities. Di Mascio et al. (2014) studied marine propeller wake instabilities using the DES method. The destabilization process of the propeller wake field was excited by the central vorticity in axisymmetric flow, while the secondary vorticity with the hub vortex was the major contributor to oblique flow. Dubbioso et al. (2013, 2014) used the RANS method to study the wake behaviors in a wide range of incidence angles (10–50°) at two different loading conditions, demonstrating that the propeller load increased almost linearly with the incidence angle and the vortex structures were complicated in oblique flow. Chase and Carrica (2013) conducted simulations of the submarine propeller E1619 for different grids and turbulence models. The results show that the mesh resolution slightly affects thrust and torque but strongly affects the wake. On the other hand, the RANS method excessively dissipated the wake and the calculated tip vortices were nonphysical.

Dynamic mode decomposition (DMD) (Jovanović et al., 2014; Schmid, 2010, 2011; Schmid et al., 2011) projects a high-dimensional data sequence (either experimentally or numerically) into a low-dimensional space and simultaneously obtains the dominant modal characteristics. Modal analysis can not only obtain the flow instability and dynamic characteristics but also reconstruct the flow field via the DMD reduced-order model (Liang et al., 2020; Liu et al., 2021a, 2021b). Therefore, DMD is an effective approach for investigating the highly complex wake past a propeller (Debnath et al., 2017). Magionesi et al. (2018) used DMD to analyze a propeller wake field. The DMD analysis showed that the evolution process of the propeller wake was dependent on the propeller loading and related to the most energetic modes, which was identified by the main frequency of the propeller wake field being consistent with the blade pass frequency and its multiples. Sun et al. (2021) and. Zhu et al. (2022) studied the unsteady wake flow of a horizontal-axis wind turbine using LES. Based on DMD analysis, the swing and rotating motion of the tip vortices were identified and the instability of the tip vortex was related to the small-scale turbulence. Liu et al. (2020) conducted DMD and reconstruction to study flow characteristics of multiphase flow in a pump and obtained the primary frequencies and the associated coherent structures. The reduced-order reconstruction fields can effectively depict the main flow features, but cannot reflect the high-order harmonic components. Han and Tan (2020) focused on coherence modes and frequencies of tip leakage vortex by using DMD. DMD can obtain the dominant frequency of the flow field and coherent structures near the trajectory of the unstable primary tip leakage vortex. It is noted that the flow field can be successfully reconstructed based on the mean flow mode and the first mode. Wang et al. (2022b) investigated the wake instability of a propeller under a heavy loading condition using DES simulation and LES. Based on modal analysis, the LES method can resolve more flow details with richer coherent structures and a wider frequency range.

A brief literature review indicates that the evolution process and instability of the propeller wake have been studied through both numerical simulations and experiments, but the wake instability mechanisms have still not been fully revealed. There are a limited number of studies about the modal analysis of the propeller wake, focusing on heavy loading conditions. Magionesi et al. (2018) analyzed the spatial shape and time scale variation of the modes under two different operating conditions. The analysis showed that the modes are related to the evolution of the propeller wake and the destabilization mechanism. Wang et al. (2022b) carried out a propeller DMD analysis under heavy loads to learn more about the initiation mechanism of propeller wake instability. Shi et al. (2022) used DMD to study the effect of nozzles on the wake flow dynamics and instability mechanism of a four-bladed marine propeller. However, modal analysis of the propeller wake under light loading conditions has been largely neglected. From the perspective of engineering application, any propulsion system designed to operate under heavy loading conditions must necessarily transit the light-to-heavy loading conditions. From a scientific standpoint, it is of great significance to provide a better insight into the propeller wake dynamics under light loading conditions via DMD. Therefore, in this paper, the propeller wake is simulated using the LES method under a light loading condition, and then DMD is used to identify the dominant frequencies and mode features of the propeller wake. Finally, a reduced-order wake field is reconstructed based on the primary modes and compared with the original wake field. This work could extend the knowledge of the propeller wake dynamics to the light loading range.

2. Research approach

2.1. Governing equations

In the Cartesian coordinate system, based on the assumption of incompressibility, the basic governing equations include the mass conservation and momentum conservation equations, i.e., the Navier-Stokes equations, which are described as follows:

$$\frac{\partial \rho}{\partial t}+\frac{\partial(\rho u_i)}{\partial x_i}=0 \tag{1}$$

$$\frac{\partial(\rho u_i)}{\partial t}+\frac{\partial\left(\rho u_i u_j\right)}{\partial x_j}=-\frac{\partial p}{\partial x_i}+\frac{\partial}{\partial x_j}\left(\mu \frac{\partial u_i}{\partial x_j}\right) \tag{2}$$

where u_i represents the velocity component in the i direction, p represents the pressure, ρ represents the density, and μ represents the flow viscosity.

When solving the propeller flow field, the large-scale vortices in the fluid domain are solved directly, while the small-scale vortices need to be modeled through the LES approach (Kumar and Mahesh, 2017). Therefore, by filtering the solution variables and inserting them into the Navier-Stokes equations, the filtered LES equation can be written as follows:

$$\frac{\partial \rho}{\partial t}+\frac{\partial \rho \overline{u}_j}{\partial x_j}=0 \tag{3}$$

$$\frac{\partial(\rho \overline{u}_i)}{\partial t}+\frac{\partial\left(\rho \overline{u}_i \overline{u}_j\right)}{\partial x_j}=-\frac{\partial \overline{p}}{\partial x_i}+\frac{\partial}{\partial x_j}\left(\mu \frac{\partial \overline{u}_i}{\partial x_j}\right)-\frac{\partial \tau_{ij}}{\partial x_j} \tag{4}$$

where the over-bars of the letter represent filtered quantities, τ_{ij} is known as the sub-grid scale (SGS) stress with the definition in Eq. (5).

$$\tau_{ij}=\rho\left(\overline{u_i u_j}-\overline{u}_i \overline{u}_j\right) \tag{5}$$

Based on the Boussinesq assumption, the SGS stress can be modeled by the eddy viscosity model as shown in Eq. (6),

$$\tau_{ij}=\frac{1}{3}\tau_{kk}\delta_{ij}-2\mu_t \overline{S}_{ij} \tag{6}$$

where τ_{kk} is the isotropic part,$\overline{S}_{ij}$ is the strain rate tensor of the resolved scale, andμ_t is the sub-grid scale turbulent viscosity. The sub-grid scale turbulent viscosityμ_t must be closured by a sub-grid scale model that considers the effect of small eddies on the resolved fluid. In this paper, μ_t is closured by the wall adapting local eddy-viscosity (WALE) model (Nicoud and Ducros, 1999), which can be defined as:

$$\mu_t=\rho \Delta_s^2 \frac{\left(S_{ij}^d S_{ij}^d\right)^{3/2}}{\left(\overline{S}_{ij}\overline{S}_{ij}\right)^{5/2}+\left(S_{ij}^d S_{ij}^d\right)^{5/4}} \tag{7}$$

$$\overline{S}_{ij}=\frac{1}{2}\left(\frac{\partial \overline{u}_i}{\partial x_j}+\frac{\partial \overline{u}_j}{\partial x_i}\right) \tag{8}$$

$$S_{ij}^d=\frac{1}{2}\left(\overline{g}_{ij}^2+\overline{g}_{ji}^2\right)-\frac{1}{3}\delta_{ij}\overline{g}_{kk}^2 \tag{9}$$

$$\overline{g}_{ij}=\frac{\partial \overline{u}_i}{\partial x_j} \tag{10}$$

The SGS mixing length Δ_s is defined as:

$$\Delta_s=\min\left(kd, C_s V^{1/3}\right) \tag{11}$$

where V represents the grid cell volume, k represents the von Kármán constant, d represents the shortest distance to the wall, and C_s represents the WALE constant. The typical values of C_s published in the literature range from 0.5 (for freely decaying isotropic homogeneous turbulence flow) to 0.325 (for channel flow). The choice $C_s = 0.5$ in this paper is suitable for the freely decaying isotropic homogeneous turbulence (Nicoud and Ducros, 1999).

2.2. Dynamic mode decomposition

DMD methods have been widely used in complex flow fields such as separation flows and wind turbine wakes flows.

The discrete flow field data are used to construct the snapshots matrix required by the DMD. The flow field data are arranged as a snapshots matrix V_1^N:

$$V_1^N=[v_1, v_2, v_3, \cdots, v_i, \cdots, v_N] \tag{12}$$

where v_i represents the i-th flow field data snapshot, and N represents the total number of flow field data snapshots. Assuming that the flow field data are linear, there is a constant linear mapping A connecting the propeller wake field v_i to the next propeller wake field v_{i+1},

$$v_{i+1}=Av_i \tag{13}$$

The snapshots matrix V_1^N can be expressed as:

$$V_1^N=\left[v_1, Av_1, A^2v_1, \cdots, A^{i-1}v_1, \cdots, A^{N-1}v_1\right] \tag{14}$$

The snapshot v_N can be represented as a linear combination, which includes previous *N-1* snapshots,

$$v_N=c_1v_1+c_2v_2+\cdots+c_{N-1}v_{N-1}+r \tag{15}$$

where $c_1, c_2, \cdots, c_{N-1}$ are the polynomial coefficient of the previous *N-1* snapshots and r represents the residual vector.

By combining Eqs. (13) and (15), we get:

$$AV_1^{N-1}=V_2^N=V_1^{N-1}S+re_{N-1}^T \tag{16}$$

where $V_1^{N-1}=[v_1, v_2, \cdots, v_{N-1}]$, $V_2^N=[v_2, v_3, \cdots, v_N]$, e_{N-1} represents the (*N-1*)-th unit vector, and the matrix S can be expressed as:

$$S=\begin{bmatrix} 0 & & & & c_1 \\ 1 & 0 & & & c_2 \\ & \ddots & \ddots & & \vdots \\ & & 1 & 0 & c_{N-2} \\ & & & 1 & c_{N-1} \end{bmatrix} \tag{17}$$

Using the QR-decomposition snapshot matrix V_1^{N-1}, y_i is an eigenvector of$S$, then $\varphi_i = V_1^{N-1}y_i$ is an approximate eigenvector of A.

Due to the limitations of QR-decomposition, singular value decomposition (SVD) is used instead of QR-decomposition to process the original flow field data:

$$V_1^{N-1}=U\sum W^* \tag{18}$$

The complete matrix is obtained from Eqs. (16) and (18):

$$\widetilde{S}=U^H V_2^N W\sum W^{-1} \tag{19}$$

where U^H is a complex conjugate transpose of the basis U, which is obtained from the singular value decomposition (SVD) of V_1^{N-1}, as shown in Eq. (18). The DMD modes can be obtained by the eigenvectors y_i, where y_i is the eigenvector of $\widetilde{S}$ with linear independence. Therefore, the DMD modes can be expressed as:

$$\varphi_i=Uy_i \tag{20}$$

Therefore, the snapshot matrix V_1^{N-1} obtained from experiments or numerical simulations can be expressed as:

$$\underbrace{[v_1, v_2, \ldots, v_{N-1}]}_{V^{N-1}}=\underbrace{[\varphi_1, \varphi_2, \ldots, \varphi_{N-1}]}_{\Phi}\underbrace{\begin{bmatrix} \alpha_1 & & \\ & \alpha_2 & \\ & & \ddots \\ & & \alpha_{N-1} \end{bmatrix}}_{D_\alpha=\mathrm{diag}(\alpha)}\underbrace{\begin{bmatrix} 1 & \mu_1 & \cdots & \mu_1^{N-1} \\ 1 & \mu_2 & \cdots & \mu_2^{N-1} \\ \vdots & \vdots & \vdots & \vdots \\ 1 & \mu_{N-1} & \cdots & \mu_{N-1}^{N-1} \end{bmatrix}}_{V_{and}} \tag{21}$$

where α_i is the amplitude, φ_i is the DMD mode, and μ_i is the eigenvalues of the eigenvectors y_i. The DMD mode φ_i can be solved by the Vandermonde matrix V_{and} of eigenvalues μ_i. The i-th amplitude represents the weight of the i-th mode, which describes the importance of various modes from the first to the last time sequence. The real part and imaginary part of each eigenvalue indicate the growing rates and frequencies of the flow field around the propeller, respectively. Each mode corresponds to a kind of flow structure. For example, the first mode indicates the averaged flow of the propeller, whose growing rate and frequency correspond to 0. The second mode usually represents the most energetic vortex evolution in time and space, so the frequency of the second mode corresponds to the fundamental frequency of the propeller. Similar analysis can be applied to the other modes.

The amplitude α_i can be solved by the optimization problem of the following equation (Chen et al., 2012; Jovanović et al., 2014; Qiu et al., 2020):

$$\min_{\alpha}\|J(\alpha)\|=\min_{\alpha}\left\|V_1^{N-1}-\Phi D_\alpha V_{and}\right\|_F^2 \tag{22}$$

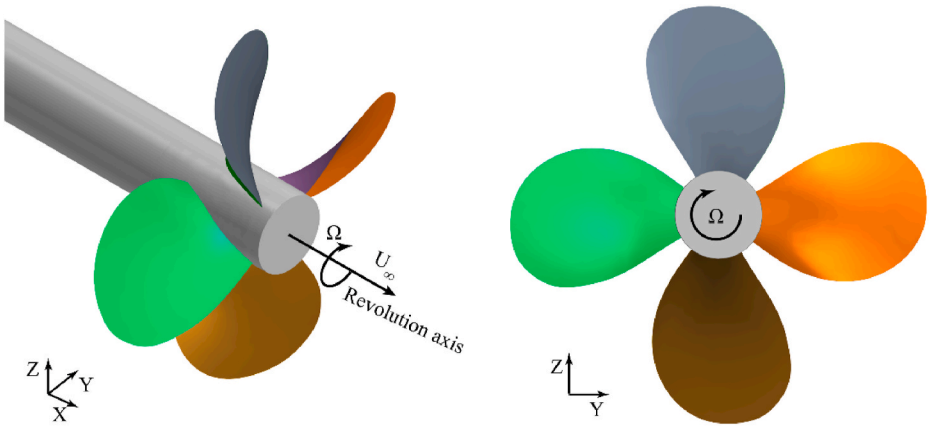

Fig. 1. Geometry and reference system of the propeller.

Table 1
Basic parameters of the INSEAN E779A propeller.

Description	Symbol	Value	Units
Number of blades	Z	4	
Radius	R	0.113635	m
Diameter	D	0.22727	m
Rotational speed	n	25	rps
Pitch ratio	P/D	1.1	
Blade passing frequency	BPF	100	Hz
Hub diameter ratio	d_h/D	0.200	
Area ratio	A_E/A_0	0.689	
Reference chord	$C_{0.7R}$	86	mm
Reference velocity	$V_{ref0.7R} = \sqrt{U_\infty^2 + (2\pi nR)^2}$	18.5 ($J = 0.85$)	m/s
Reynolds number	$Re_{0.7R} = \frac{C_{0.7R} V_{ref0.7R}}{\nu}$	1.14×10^6 ($J = 0.85$)	

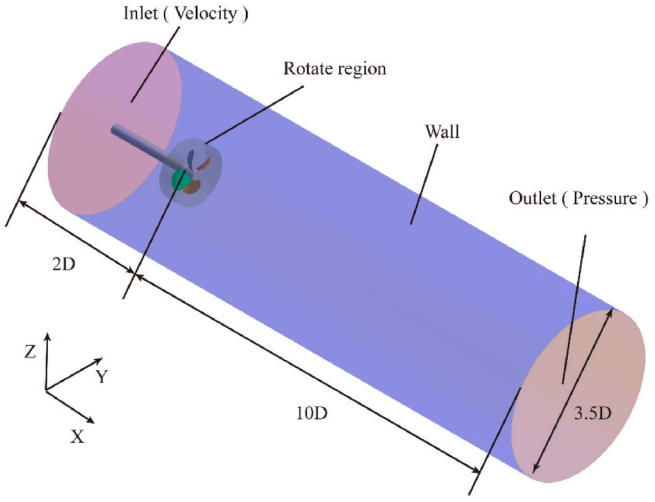

Fig. 2. Computational domain and boundary conditions.

where $\varphi = [\varphi_1(x), \varphi_2(x), \cdots, \varphi_{N-1}(x)]$ and $D_\alpha = \mathrm{diag}(\alpha)$ represents the diagonal matrix of the vector $\alpha = [\alpha_1, \alpha_2, \cdots, \alpha_{N-1}]$.

3. Numerical simulation

3.1. Test case

In this paper, the E779A propeller was chosen as the research object, and the model agrees with the experimental model (Felli et al., 2008, 2011). The propeller geometry and propeller coordinate system are shown in Fig. 1, with the coordinate origin at the center of the propeller. The main parameters of the propeller geometry are listed in Table 1. The INSEAN E779A propeller is widely used to investigate the propeller wake (Felli et al., 2008, 2011; Felli and Falchi, 2018; Felli and Felice, 2005).

The light loading condition $J = 0.85$ was simulated, where the advance coefficient (J) is represented as $J = U_\infty/nD$, with $n = 25rps$ and $D = 0.227m$. Based on previous experiments and numerical calculations (Ahmed et al., 2020; Felli et al., 2011), it can be found that the wake vortex system of the INSEAN E779A propeller is stable when the advance coefficient is $J = 0.85$, and the wake vortex system maintains an orderly structure and regular motion during the downstream movement. Therefore, the propeller wake field is considered to be a periodic flow, and the dominant frequencies and modal characteristics of the wake field can be obtained by DMD.

To resolve more accurate vortex structures in the propeller wake, the unsteady governing equations are iteratively solved using the SIMPLE algorithm. The spatial term is discretized using the second-order upwind scheme, the temporal term is discretized using the second-order implicit scheme, and a central difference method is utilized for the convection term. The time-step in the numerical calculation is set to $\Delta t = 1.1111 \times 10^{-4}$s, that is, the propeller rotates 1° in one time-step during the calculation process (Sun et al., 2020).

3.2. Mesh details

As shown in Fig. 2, the computational domain is a cylinder with a diameter of 3.5D, where D is the propeller diameter. The inlet plane is 2D from the propeller center and the outlet plane is 10D from the propeller center. The size of the computational domain is consistent with the experiments and the computational domain can be considered to have no constraining effects in numerical simulations (Kumar and Mahesh, 2017). The inlet was set as the inlet velocity, according to $J = 0.85$, the outlet was set as the pressure outlet, and the other boundary conditions of the computational domain and the propeller wall were set as no-slip walls.

In this paper, an unstructured Cartesian mesh (Hu et al., 2021; Wang et al., 2018, 2019) is used. To resolve the wake details past the propeller, multiple cylindrical control bodies are used to refine the mesh in the propeller region. The control bodies are distributed around the propeller as shown in Fig. 3(a), mainly including the tip vortex refining region and the hub refining region. The grid distribution is shown in Fig. 3(b). First, surface remeshing is performed on the propeller surface. Then a high-quality surface mesh with good surface triangulation is generated. Finally, the volume mesh with prism layer mesh and trimmed mesh is

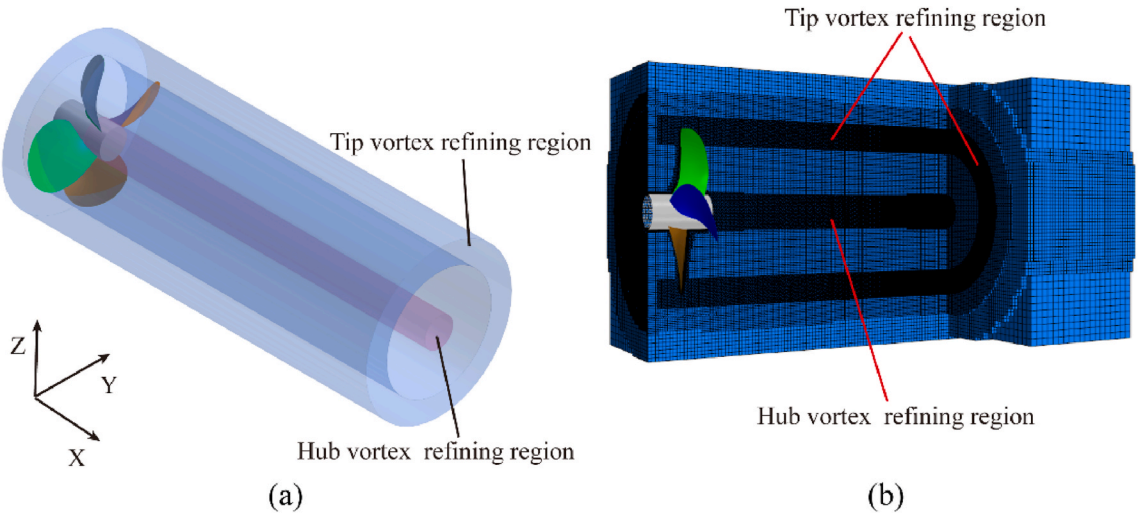

Fig. 3. Refining region and refining mesh of the propeller, (a) refining region, (b) local refining mesh.

Table 2
Grid convergence analysis ($J = 0.85$).

	Medium	Fine	Exp.	Err m_{ed} (%)	Err $_{fine}$ (%)	E	U_N (%)
K_T	0.1732	0.1725	0.1659	4.40	3.98	1.36×10^{-3}	0.47
$10K_Q$	0.3364	0.3362	0.3358	0.18	0.12	3.64×10^{-3}	0.18

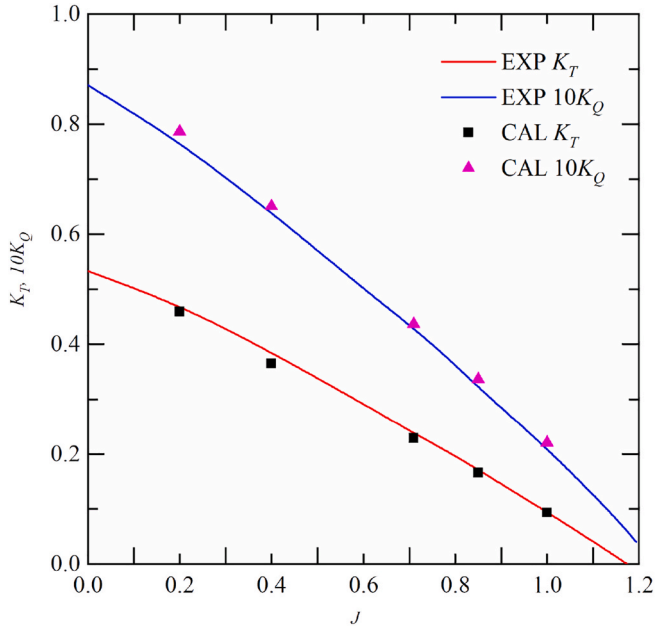

Fig. 4. Open water characteristics of the experiments (Ahmed et al., 2020; Felli et al., 2011) and calculated results.

generated based on the surface mesh. For the mesh along the wall, the boundary layer was set to 20 layers with the boundary layer growth rate of 1.2, and the total thickness of the boundary layer was set to 0.00023m. To meet the requirements of LES calculation accuracy, y^+ is set to be less than 1, as suggested by Di Mascio et al. (2014).

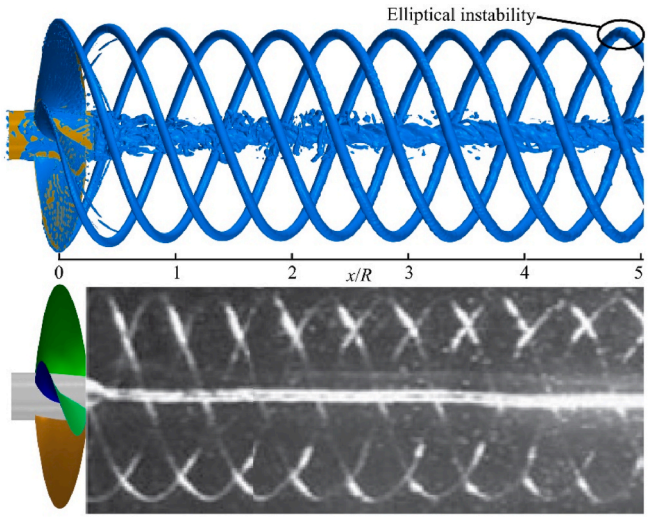

Fig. 5. Comparison of the propeller wake between the numerical calculation and the experiment (Felli et al., 2011) (Top: calculation; bottom: experiment).

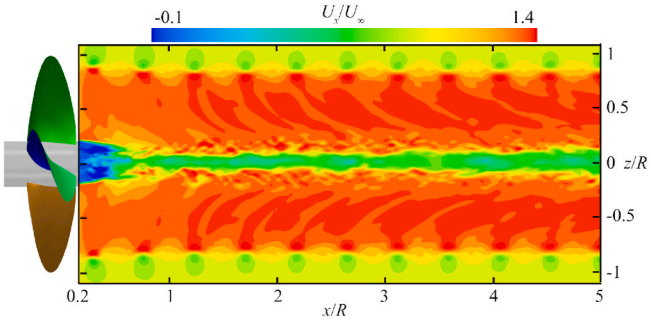

Fig. 6. Instantaneous axial velocity distribution on the central-longitudinal plane ($t = 1.00$T). The axial velocity U is normalized with U_∞.

3.3. Verification and validation

To evaluate the numerical uncertainty, uncertainty analysis is carried out on the calculation grid. The analysis process is consistent with that of Sun et al. (2020). We use a Cartesian grid to divide the medium

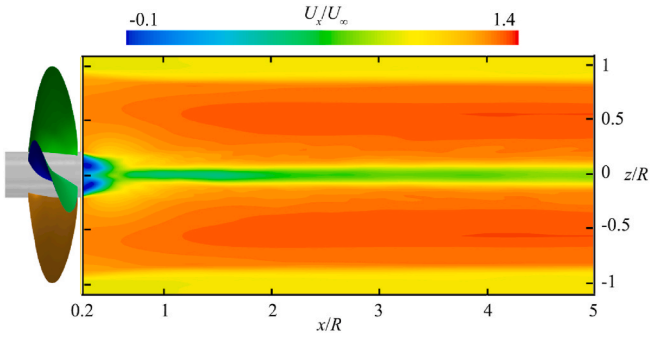

Fig. 7. Time-averaged axial velocity on the central-longitudinal plane.

grids and the fine grids. The mesh refinement rate (Gong et al., 2021; Sun et al., 2022) for medium and fine grids is defined as:

$$r = \left(\frac{N_{fine}}{N_{medium}}\right)^{1/d} \tag{23}$$

where N_{fine} represents the total number of fine grids with the value of 14.10 million, N_{medium} represents the total number of medium grids with the value of 8.45 million, and$d$ represents the simulation dimension with the value of $d = 3$. The mesh refinement rate used in this study was $r = 1.2$, as suggested by Sun et al. (2020). After the calculation is stable and converged, the thrust coefficient K_T and torque coefficient K_Q are calculated, where K_T and K_Q are defined as follows:

$$K_T = \frac{T}{0.5\rho n^2 D^4}, K_Q = \frac{Q}{0.5\rho n^2 D^5} \tag{24}$$

The error between the two sets of grids is expressed as:

$$E = \frac{f_{medium} - f_{fine}}{1 - r^p} \tag{25}$$

where p represents the formal order of accuracy, with $p = 2$, f_{fine} represents the calculated result of the fine grids, and f_{medium} represents the calculated result of the medium grids. The uncertainty of the propeller load is estimated by:

$$U_N = F_S|E| \tag{26}$$

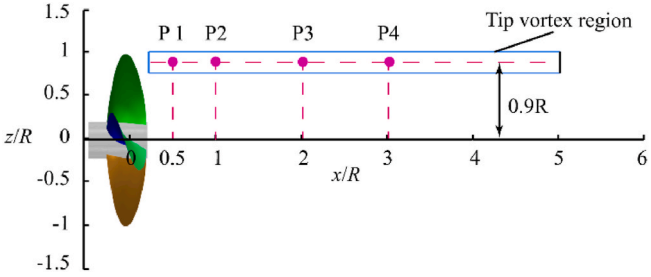

Fig. 9. Schematic diagram of the monitoring point location.

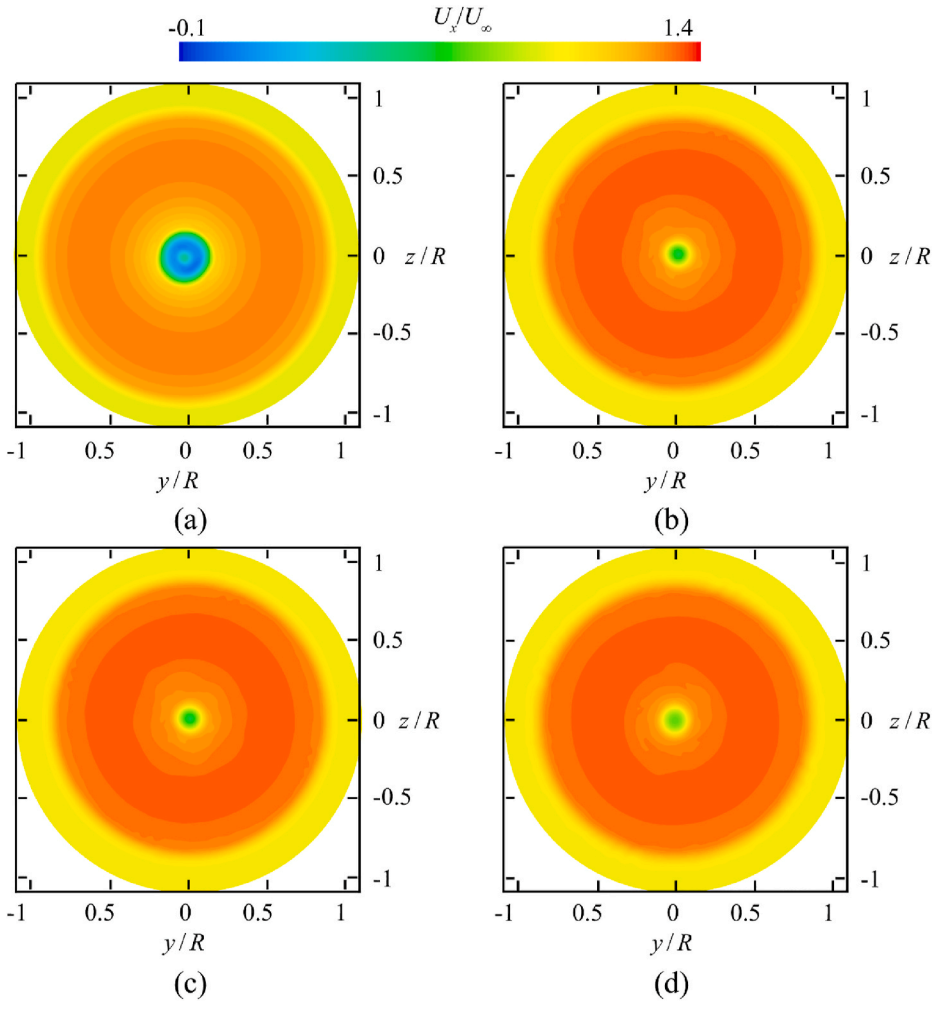

Fig. 8. Time-averaged axial velocity on various transverse planes: (a) $x = 0.5R$, (b) $x = 1.0R$, (c) $x = 2.0R$, (d) $x = 3.0R$.

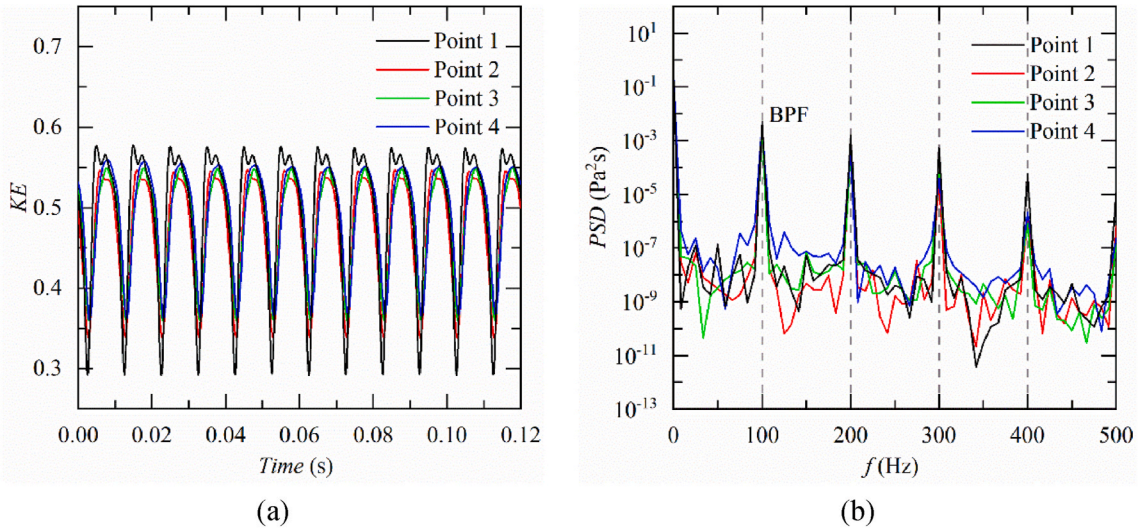

Fig. 10. (a) The kinetic energy (KE) and (b) the power spectrum distribution (*PSD*) of four monitoring points.

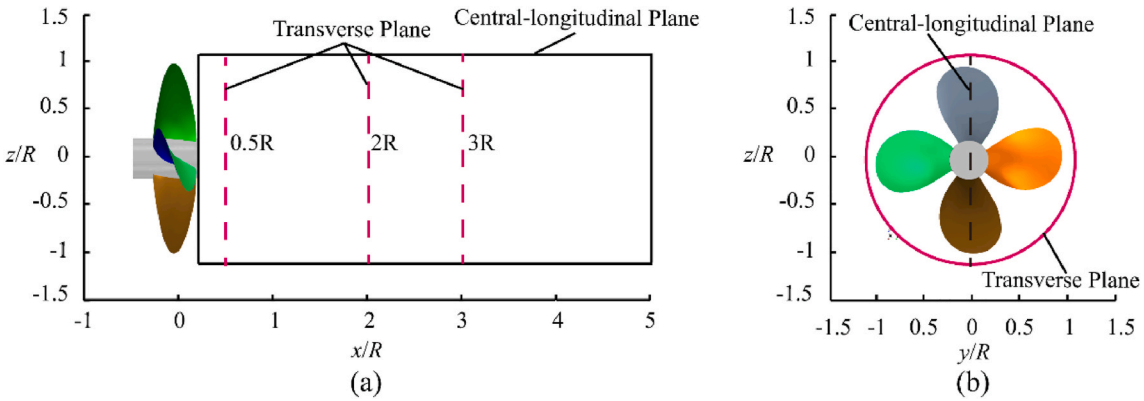

Fig. 11. Planes for snapshot data acquisition, (a) front view, (b) side view (Black solid line: central-longitudinal plane; pink dashed line: transverse planes). (For interpretation of the references to colour in this figure legend, the reader is referred to the Web version of this article.)

where F_S represents a safety factor, with $F_S = 3$.

Table 2 shows the results of grid convergence analysis based on K_T and K_Q. The calculated results for the fine and medium grids are in good agreement with the experimental results (Ahmed et al., 2020; Felli et al., 2011). The errors of K_T and K_Q under the medium grid are 4.4% and 0.18%, and the errors of K_T and K_Q under the fine grid are 3.98% and 0.12%. The load errors of the two grids are both less than 5%. It is worth noting that the calculated results of the fine grids are closer to the experimental results. At the same time, the uncertainties of the calculated K_T and K_Q are 4.4% and 0.18%, respectively. The uncertainty of propeller load is less than 3%, so the two sets of grids can be considered reliable (Di Mascio et al., 2014). This study uses fine grids to capture the detailed features of the wake passing through the propeller blades, the fine grids are finally selected in this study. The open water characteristics calculated by the fine mesh are shown in Fig. 4. The calculated K_T and K_Q are consistent with the experimental results, so the fine mesh is fully competent for the simulation tasks in this study.

4. Results

4.1. Wake field characteristics

Fig. 5 shows the propeller wake obtained by the numerical calculation and the experiment. The propeller wake is visualized by the vortex structures by using the isosurface of the Q criterion (Wang et al., 2020), where $Q = 20000\ s^{-2}$. The calculated results are consistent with the experimental results. The calculated tip vortices are the same as those observed experimentally, the position of the tip vortex structure is the same as the experimental one, and the hub vortex develops straight backward. The vortex system topology of the propeller wake includes regular tip vortices and hub vortex, and elliptical instabilities are captured downstream of the tip vortices. Since the tip vortices and the hub vortex do not interfere with each other, the wake vortex structures are stable within the visualization range. The tip vortices retain their geometric characteristics (pitch and tip-to-tip distance). The difference in the hub vortex structure is mainly due to an ellipsoidal body being used for the tail of the propeller hub in the experiments (Felli et al., 2011) while a blunt hub is used in the numerical calculations. According to previous studies in the literature (Magionesi et al., 2018), the flow is mainly associated with the ordered convection of the tip vortex while the hub vortex dynamics have a negligible contribution. Therefore, the change in hub geometry has little effect on the DMD analysis of the propeller wake flow under light load conditions.

Fig. 6 shows the instantaneous axial velocity distribution on the central-longitudinal plane. It is observed that the velocity in the region between the tip vortex and the hub vortex is higher than that in the free stream, this region has a high-velocity sheet region due to the influence of the propeller blade boundary layer (Ahmed et al., 2020), and the velocity of the hub vortex region is lower. The axial velocity in the tip vortex region shrinks and expands alternately. This is mainly because

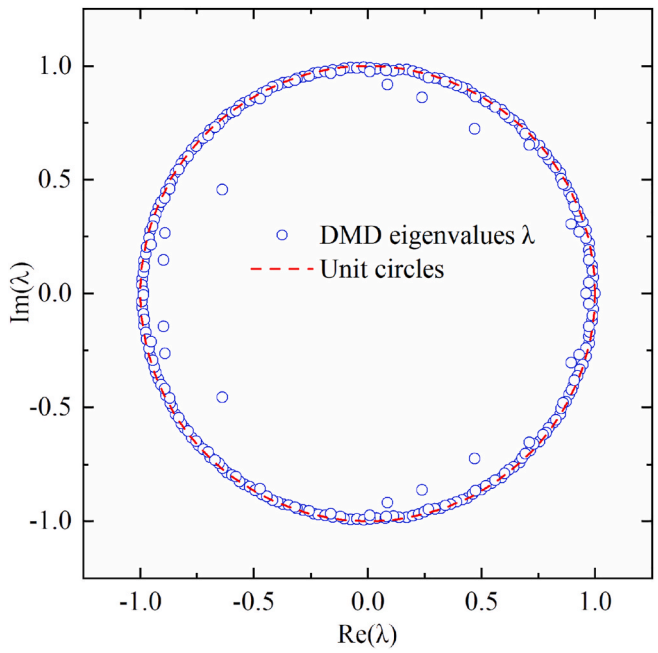

Fig. 12. Distribution of eigenvalues obtained by DMD (central-longitudinal plane).

when the fluid passes through the tip vortex, the velocity gradient changes dramatically, and then the velocity recovers after passing through the tip vortex.

Time-averaged axial velocity distribution on the longitudinal plane and various transverse planes are shown in Figs. 7 and 8, respectively. Consistent with the instantaneous velocity distribution in Fig. 6, the time-averaged axial velocity in the region between the tip vortex and the hub vortex is higher than that of the free stream, and the time-averaged axial velocity of the hub vortex is lower than that of the free stream. The flow augments in the near-wake flow field of the propeller and the wake contraction can be observed (Kumar and Mahesh, 2017). It can be seen from Fig. 8 that the time-averaged axial velocity at $x = 0.5R$ is smaller than in other positions due to the influence of the propeller blades and hub. When $x > 1.0R$, the time-averaged axial velocity is distributed similarly at various transverse planes, indicating that the propeller wake is stable within the visualization range.

To better analyze the propeller wake dynamics, the kinetic energy (KE) of the propeller wake field is extracted, and the positions of monitoring points are shown in Fig. 9. The radial position of the monitoring points is $z/R = 0.9$, located mainly in the propeller tip vortex region. The axial positions of the monitoring points are $x/R = 0.5$, 1, 2,

Table 3
Dominant frequencies obtained by DMD and FFT.

Mode	DMD	FFT	Error
1	0	0	–
2	99.90	100	0.10%
3	200.03	200	0.02%
4	299.99	300	0.003%

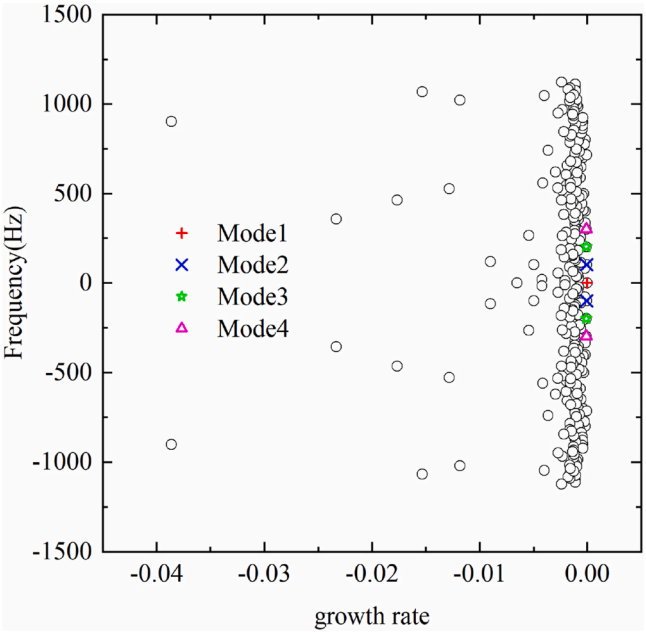

Fig. 14. Growth rate and frequency of DMD modes.

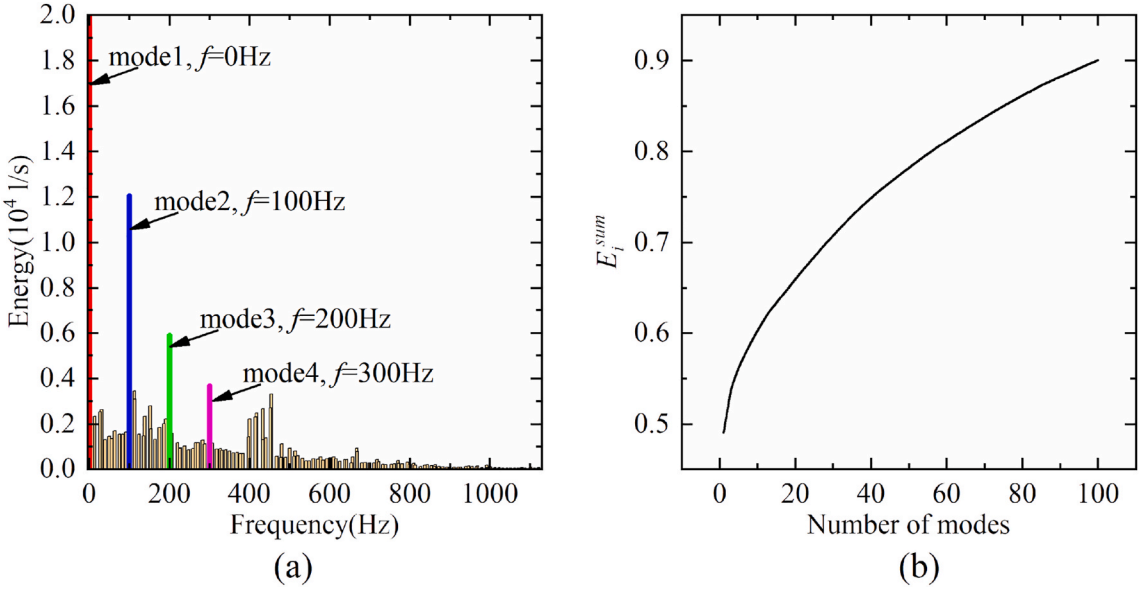

Fig. 13. (a) Energy distribution, (b) cumulative energy at central-longitudinal plane.

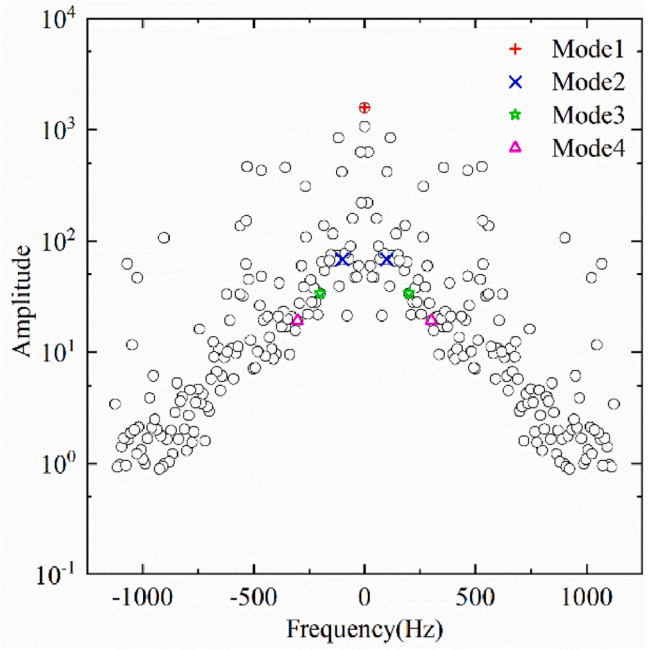

Fig. 15. Amplitude and frequency of DMD modes.

3, located near and in the middle portion of the propeller wake.

Fig. 10 shows the *KE* and the power spectrum distribution (*PSD*) of the monitoring points. The *KE* (Felli and Falchi, 2018) is defined as $KE = 0.5(u^2 + v^2 + w^2)/U_\infty^2$, where u, v, w are the velocity components along three orthogonal axes, and U_∞ is the inlet velocity. It is noted that the *KE* amplitude varies widely near the propeller, which is due to the stronger induced velocity caused by the propeller rotation. Downstream from the propeller, these induced velocities are almost the same, so the *KE* amplitude varies similarly at points 2–4.

Fig. 10(b) shows the *KE*-normalized power spectrum distribution of monitoring points. The blade passing frequency is defined as $BPF = nZ = 100$Hz, where $n = 25rps$ is the rotational speed and $Z = 4$ is the number of propeller blades. The main peaks appear at the blade passing frequency and their integer multiples, demonstrating that the velocity fluctuation of the propeller wake is mainly related to the rotation of the propeller.

4.2. DMD analysis for the wake field

To analyze the wake dynamics, the velocity fields are extracted at one central-longitudinal plane and three transverse planes (i.e., $x = 0.5R$, $x = 2.0R$, and $x = 3.0R$), as shown in Fig. 11. Fig. 10 shows that the high-frequency components in the wake field occupy less energy, so the snapshot frequency $f_s = 1/\mathrm{dt} = 2250$Hz can meet the DMD requirements, where the time interval is set to $dt = 4\Delta t = 4.4444 \times 10^{-4}$s (that is, four times the time-step). Following the recommendations given by Sun et al. (2021) for DMD analysis of rotating machinery, we sampled temporal data for nine rotation cycles and obtained 810 snapshots of the velocity field. The resultant sampling frequency meets the Nyquist–Shannon criterion (Magionesi et al., 2018; Shannon, 1949). The three velocity components (U_x, U_y, U_z) at the cross section are extracted as original data and used as the input to the DMD program to obtain the corresponding DMD results. According to the previous literature (Ahmed et al., 2020; Kumar and Mahesh, 2017), the propeller wake instability is mainly manifested in the axial velocity, so we only show the DMD results via the cloud diagram of the axial velocity (U_x). We reconstructed the reduced-order wake field by using the primary modes, but the axial velocity (U_x) field is only depicted and compared with the original U_x wake field. It is noted that the DMD results are obtained using three velocity components (U_x, U_y, U_z). In addition, the DMD results are more accurate based on the three velocity components (U_x, U_y, U_z), compared with a single velocity component (U_x) as DMD raw data.

4.2.1. Central-longitudinal plane

The axial velocity on the central-longitudinal plane is analyzed by DMD. Fig. 12 shows the distribution of the unit circle and eigenvalues, where the red dotted line is the unit circle, and the blue circle are the DMD eigenvalue. The horizontal axis represents the real part of the eigenvalue and the vertical axis represents the imaginary part of the eigenvalue. The unit circle represents the stability of the eigenvalues. It is observed that most of the eigenvalues are on the unit circle, and a few eigenvalues are inside the unit circle, which indicates that these modes are convergent or periodic.

The DMD energy spectrum of the central-longitudinal plane is shown

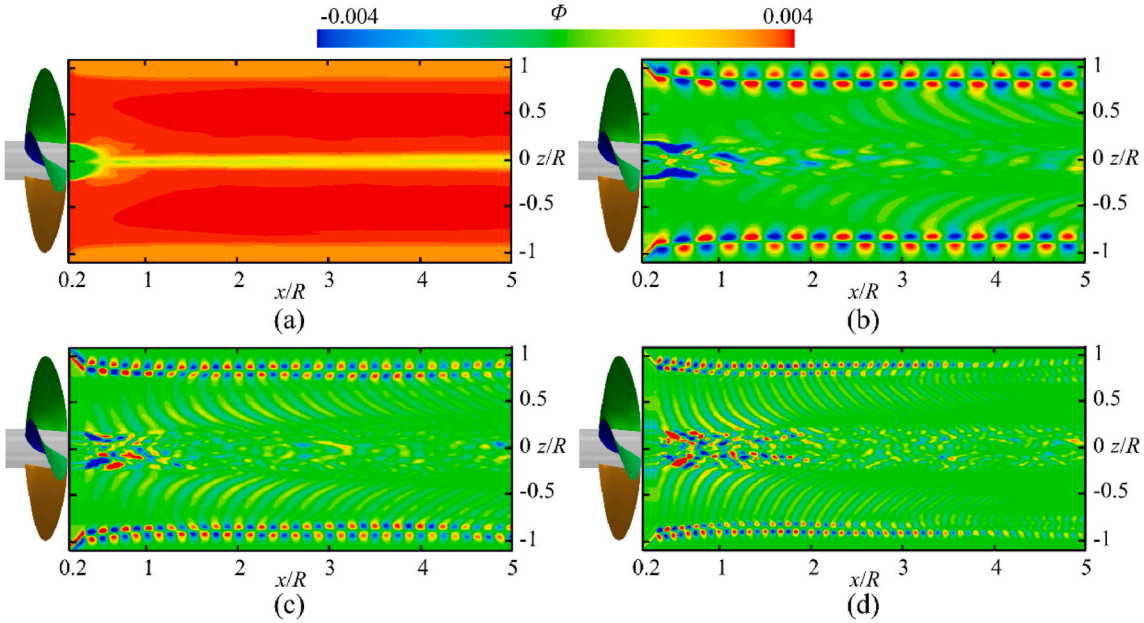

Fig. 16. The first four DMD modes of the propeller wake field: (a) mode 1, (b) mode 2, (c) mode 3, and (d) mode 4.

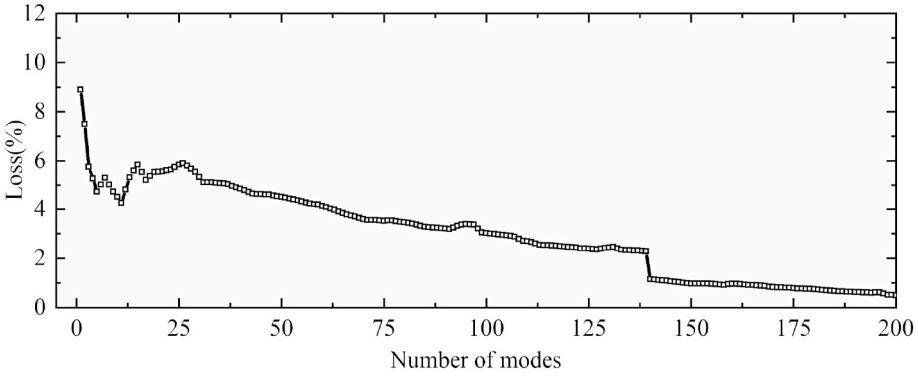

Fig. 17. The relationship between the loss function and the selected number of modes.

in Fig. 13(a). Fig. 13(b) presents the cumulative energy of the DMD mode. The eigenvalues μ_i provide the energy of the i-th DMD mode. The cumulative energy up to the i-th mode is defined as $E_i^{cum} = \sum_{k=1}^{i}\mu_k / \sum_{j=1}^{N}\mu_j$. According to the criteria for selecting modes proposed in the literature (Qiu et al., 2020), the first four modal frequencies are $f_1 =$ 0Hz, $f_2 = BPF = 100$Hz, $f_3 = 2BPF = 100$Hz, and $f_4 = 3BPF = 300$Hz, where BPF is the blade passing frequency. The frequencies obtained by DMD are in good agreement with those obtained by FFT, as shown in Table 3. The first four modes account for 54.96% of the total energy of the flow field, and mode 1 accounts for 49.06%, making it the mode with the largest energy. As the number of modes increases, the accumulated energy of the first 100 modes accounts for 90.03% of the total energy.

Fig. 14 shows the growth rate and frequency of the DMD modes, and Fig. 15 shows the amplitude and frequency of DMD modes. The growth rate g_i is defined as $g_i = \mathrm{Re}\{\log(\mu_i)\}/dt$ and the physical frequency ω_i is defined as $\omega_i = \mathrm{Im}\{\log(\mu_i)\}/dt$, where μ_i represents the eigenvalues, and dt is the time interval. The frequencies are distributed symmetrically due to complex conjugate pairs of eigenvalues. The eigenvector amplitude and the growth rate of the modes are two important parameters for selecting the dominant modes. The dominant modes have near-zero growth rates and large amplitudes. The distribution of eigenvalue amplitudes shows that DMD does not only focus on the amplitudes when looking for the main modes of the flow field but also identifies the modes that have the greatest impact on the entire time history of the flow field. The relationship between the frequency and the growth rate indicates the growth or decay of the mode over time. The growth rate of modes 1–4 are zero, indicating that modes 1–4 are stable modes and exhibit periodicity.

Fig. 16 shows the coherent structures of the first four DMD modes. It is shown that the DMD mode captures a very complex vortex system consisting of tip vortices and hub vortices. Modes 2–4 show that the coherent structures are mainly related to the ordered convection of the tip vortices, which is manifested in the fact that the dominant modal frequencies of the DMD are the blade pass frequencies and frequencies related to their multiples, while the hub vortices are less affected.

Mode 1 represents the mean flow, consistent with the flow field in Fig. 7, and mode 1 has the maximum energy. The mode 2 frequency is consistent with the dominant frequency of the propeller wake, which is the primary factor affecting the periodic flow of the propeller wake, and the mode 2 energy is the second largest. Mode 2 depicts antisymmetric large-scale structures in the tip vortex region, which is mainly related to the tip vortex structure. As the frequency increases, modes 3–4 in the tip vortex region decompose into smaller antisymmetric turbulent coherent structures, and those small coherent structures are mainly related to the small-scale vortex structures induced by the tip vortices.

DMD can reconstruct the propeller wake field by using reduced-order modes. The error of the reconstructed propeller wake field is related to the selected number of modes, which is evaluated by the loss function:

$$loss = \frac{\left\| V_1^{N-1} - \Phi D_\alpha V_{\mathrm{and}} \right\|_F}{\left\| V_1^{N-1} \right\|_F} 100\% \tag{27}$$

Fig. 17 shows the *loss* between the reconstructed propeller wake field and the original propeller wake field. As the number of modes increases, the *loss* tends to decrease. When the number of selected modes is 200, the reconstructed propeller wake field has an error of 0.5% compared with the original propeller wake field. It is worth noting that mode 1 contains most of the information about the propeller wake field, with an error of 8.89% compared to the originally simulated data. Additionally, the propeller wake field reconstructed by using the first four modes has an error of 5.26% relative to the original data sequences. On a small range, with the increase in the number of modes, the accuracy of the reconstructed propeller wake field has not been greatly improved. The propeller wake is a complex physical field with a highly complex turbulent flow structure. Although the tip vortex is an ordered flow under light load conditions, it also has the tip vortex elliptical instability and the fluctuating behavior of the hub vortex. Therefore, even if the propeller wake is a quasi-periodic process, the nonlinear characteristics of the propeller wake cannot be ignored. The loss defined in this paper is achieved by comparing the real velocity field with the reconstruction field in each time sequence, while the choosing rule of the mode is set according to the total energy of the flow field. Due to the fluctuation of the flow field in time, the addition of higher modes to the original flow fields may not decrease the loss, so the loss will increase when increasing the number of modes. When the number of modes is sufficiently large, the error induced by the inconsistency of the loss and sorting method can thus be eliminated.

Taking into account the accuracy and efficiency of the reconstruction, we take the first four modes to reconstruct the propeller wake, as shown in Fig. 18. The flow fields are reconstructed in five instances. DMD modes are ordered by their amplitudes (entries of vector α), and the flow field at any time instant is given by:

$$v_i^{rec} = \sum_{j=1}^{N-1} \varphi_j \left(\mu_j\right)^{i-1} \alpha_j \tag{28}$$

where v_i^{rec} represents the reconstructed velocity fields. The reconstructed errors at different instants are used to quantify the accuracy of the reconstructed flow fields:

$$Error(rec_i) = \frac{\left\| v_i^{CFD} - v_i^{rec} \right\|_2}{\left\| v_i^{CFD} \right\|_2} 100\% \tag{29}$$

In Fig. 18, the left side shows the original flow field during one blade passing cycle, and the right side shows the reconstructed propeller wake field. The reconstructed propeller wake field is in good agreement with the original propeller wake field. The reconstructed propeller wake field can capture the main flow characteristics of the propeller wake field,

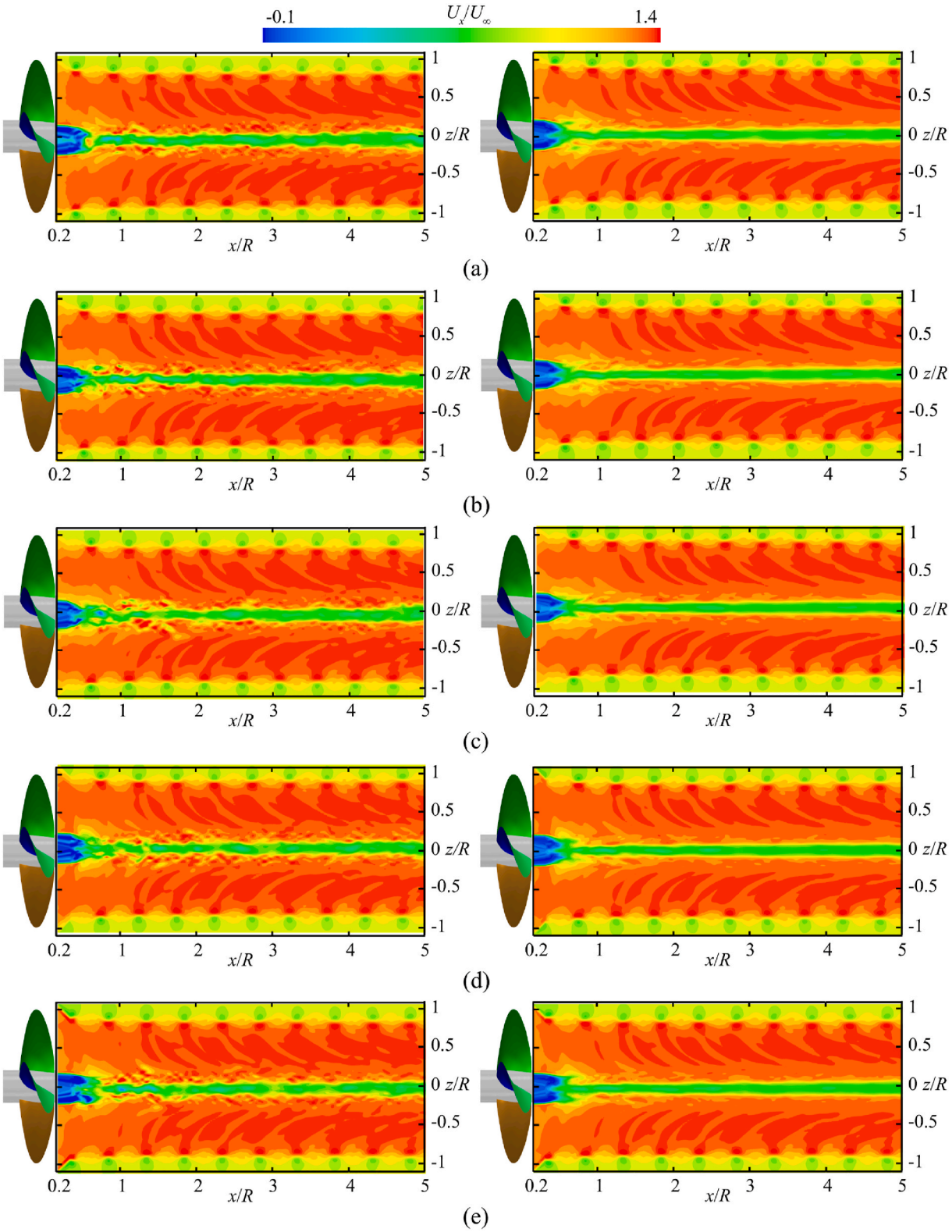

Fig. 18. The reconstructed and originally simulated axial velocity field at several instants: (a) t = 0.2T, (b) t = 0.4T, (c) t = 0.6T, (d) t = 0.8T, (e) t = 1.0T. (Left: original flow field; right: reconstructed flow field.).

Table 4
Reconstruction errors at different instants.

t	0.20T	0.40T	0.60T	0.80T	1.00T
Error (%)	5.91	4.82	4.81	5.69	5.19

such as tip vortices, hub vortices, and the thin vortex sheet that sheds off from the blade trailing edge. The reconstruction errors are listed in Table 4, the maximum error of the reconstructed propeller wake field is 5.91% at t=0.2T, the minimum error of the reconstructed propeller wake field is 4.81% at t=0.6T, and the mean error of the reconstructed

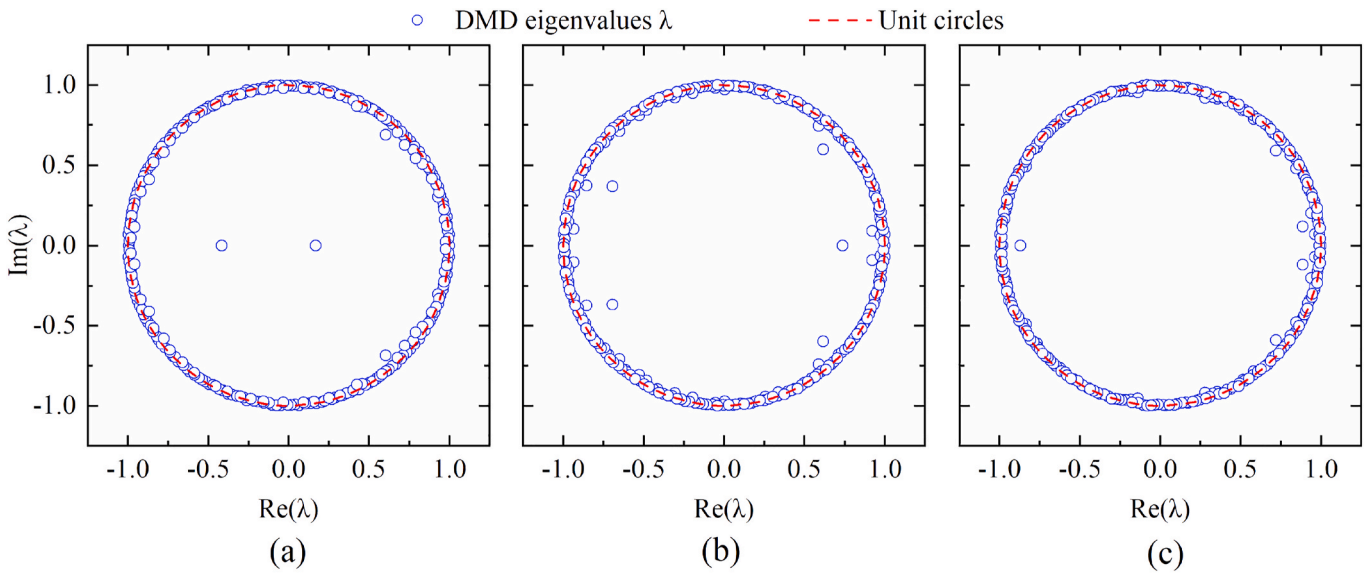

Fig. 19. Distribution of eigenvalues at three transverse planes: (a) $x = 0.5R$, (b) $x = 2.0R$, (c) $x = 3.0R$.

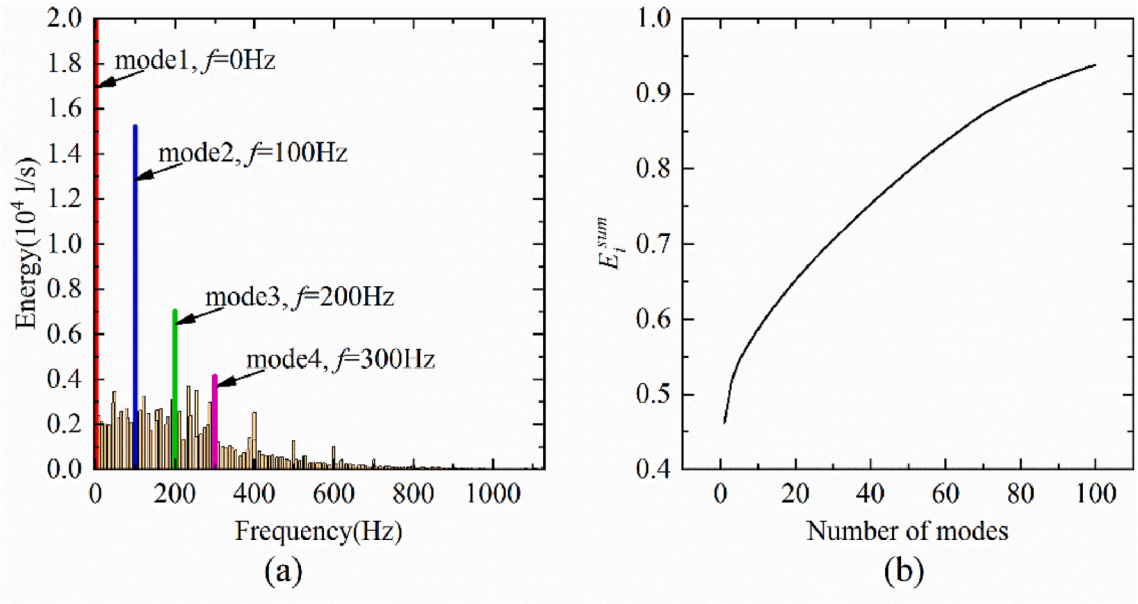

Fig. 20. (a) Energy distribution, (b) cumulative energy at $x = 0.5R$ (transverse plane).

propeller wake field is 5.28%. This is mainly because the present hub vortex contains high-frequency information, which was not included in the reconstructed propeller wake field.

4.2.2. Transverse planes

DMD is used for the dynamics of the propeller wake at three transverse planes: $x/R = 0.5$, $x/R = 2.0$, and $x/R = 3.0$. The eigenvalue distribution and energy distribution on the transverse planes are shown in Fig. 19–22. The DMD mode on the transverse planes is stable; indicating that the vortical wake develops periodically. At the planes $x/R = 0.5$, $x/R = 2.0$, and $x/R = 3.0$, the accumulated energy of the first 100 modes accounts for 93.81%, 94.27%, and 95.05%, respectively; the accumulated energy of the first four modes accounts for 53.19%, 71.09%, 72.75%, respectively; and mode 1 accounts for 46.19%, 63.83%, and 65.16% of the total energy of the flow field, respectively. At $x/R = 0.5$, the accumulated energy of mode 1 is the smallest, because the hub vortex has a high-frequency coherent structure near the propeller that decreases as the hub vortex moves downstream. Table 5 compares the dominant frequencies obtained by DMD and FFT. The frequencies obtained by DMD are consistent with those obtained by FFT. Compared with the frequencies at the central-longitudinal plane listed in Table 3, the frequencies are the same at the three transverse planes.

Fig. 23 shows the relationship between the frequency and the growth rate of DMD modes. Fig. 24 shows the amplitude-frequency relationship for all eigenvectors on the transverse planes at $x/R = 0.5$, $x/R = 2.0$, and $x/R = 3.0$, respectively. The growth rate and amplitude distribution of the modes at different transverse positions are consistent, indicating that the coherent structure in the propeller wake remains unchanged as it flows downstream. Most of the modes are concentrated where the growth rate is zero, indicating that the propeller wake is stable and exhibits periodicity.

Fig. 25 shows the coherent structures of the first four DMD modes at $x/R = 0.5$, $x/R = 2.0$, and $x/R = 3.0$. Mode 1 is the mean flow at different locations, which is consistent with the velocity distribution in

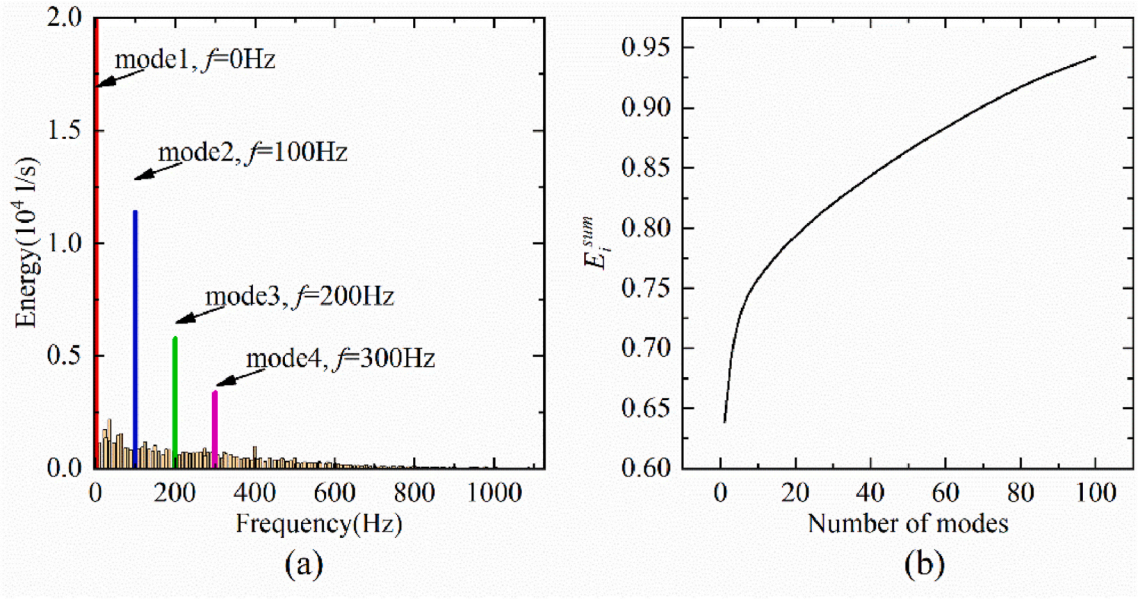

Fig. 21. (a) Energy distribution, (b) cumulative energy at $x = 2.0R$ (transverse plane).

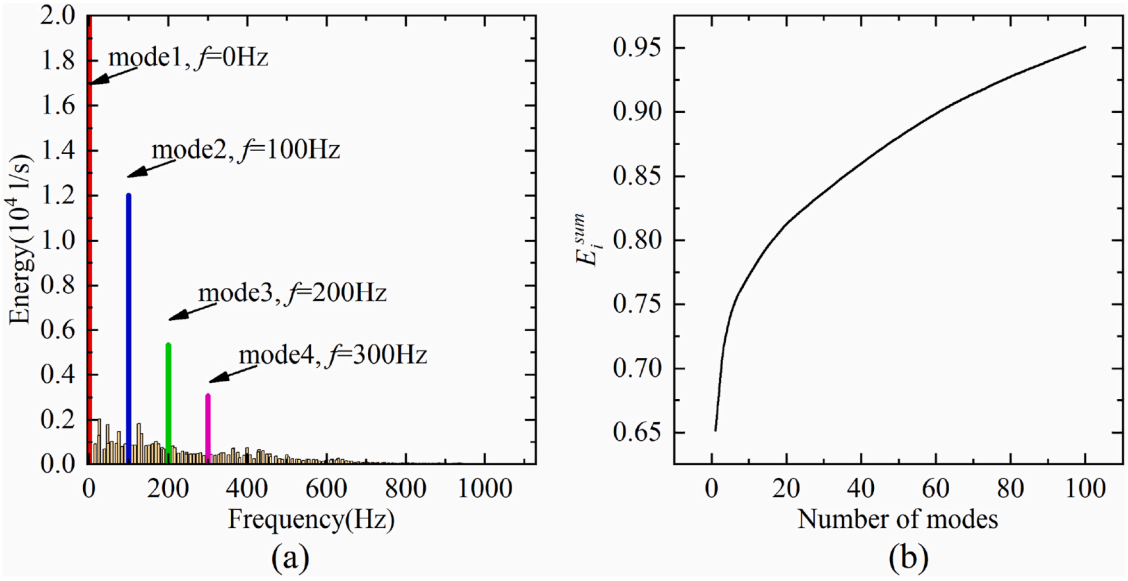

Fig. 22. (a) Energy distribution, (b) cumulative energy at $x = 3.0R$ (transverse plane).

Table 5
Comparison of dominant frequencies obtained by DMD and FFT.

Mode	$DMD_{0.5R}$	$DMD_{1.0R}$	$DMD_{2.0R}$	FFT
1	0	0	0	0
2	100.04	99.99	99.97	100
3	200.01	200.00	199.98	200
4	300.05	299.99	299.96	300

Fig. 8. Mode 2 is the large-scale structure associated with the ordered convection of the tip vortices, which remains stable in the far field of the propeller. As the frequency increases, modes 3–4 are decomposed into small-scale structures. In addition, small coherent structures are mainly related to the small-scale vortex structures induced by the tip vortices. Based on comparisons of the hub vortex at different positions, the coherent structures are obvious near the hub vortex at $x/R = 0.5$, while the coherent structures gradually decrease at $x/R = 2.0$ and $x/R = 3.0$. The DMD modes of the propeller wake at different transverse planes are mainly related to the ordered convection of the tip vortex, and its spatial wavelengths and frequencies are related to the blade passing frequency and its multiples, while the dynamics of the hub vortex have a very small contribution.

Fig. 26 shows the error between the reconstructed flow field and the original flow field, which is evaluated by the loss function in Eq. (27). Note that the error is related to the number of modes participating in the reconstruction. When the number of modes reaches 100, the errors at different transverse planes are reduced to less than 3%. It is worth noting that at $x/R = 0.5$, the reconstruction error is significantly higher than that at $x/R = 2.0$ and $x/R = 3.0$, mainly due to the hub vortex having high-frequency coherent structures that gradually decrease as the fluid flows downstream. As with the central-longitudinal plane, the first four modes are selected to reconstruct the flow field at different locations.

Figs. 27–29 are the reconstructed and originally simulated axial velocity field at $x/R = 0.5$, $x/R = 2.0$, and $x/R = 3.0$, where the upper

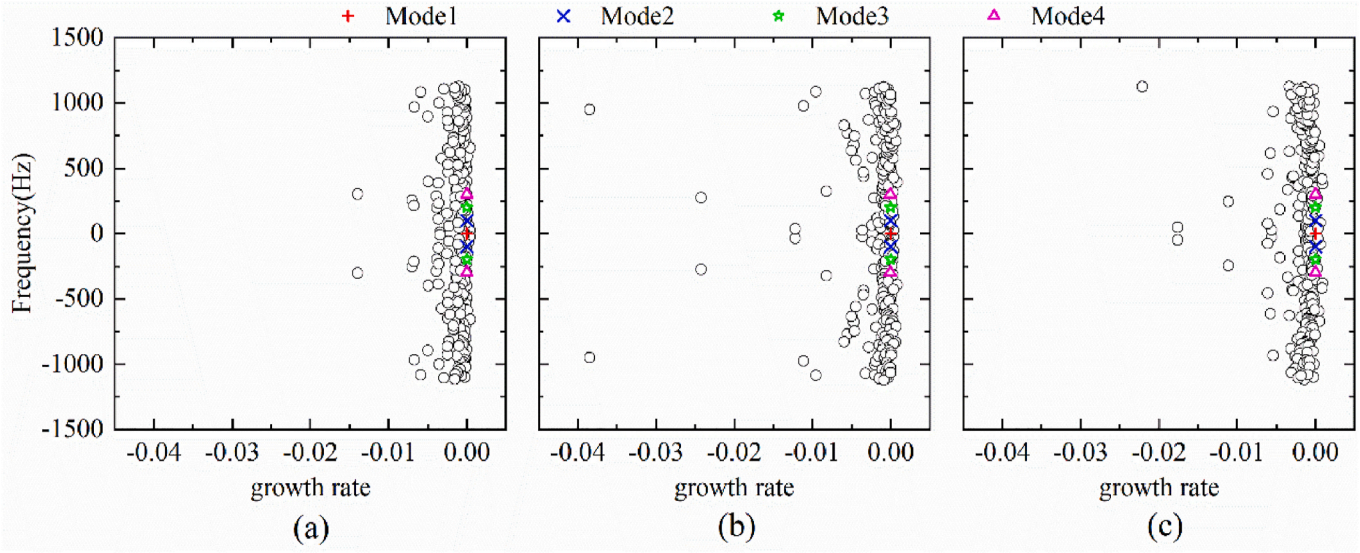

Fig. 23. Growth rate and frequency of DMD modes: (a) $x = 0.5R$, (b) $x = 2.0R$, (c) $x = 3.0R$.

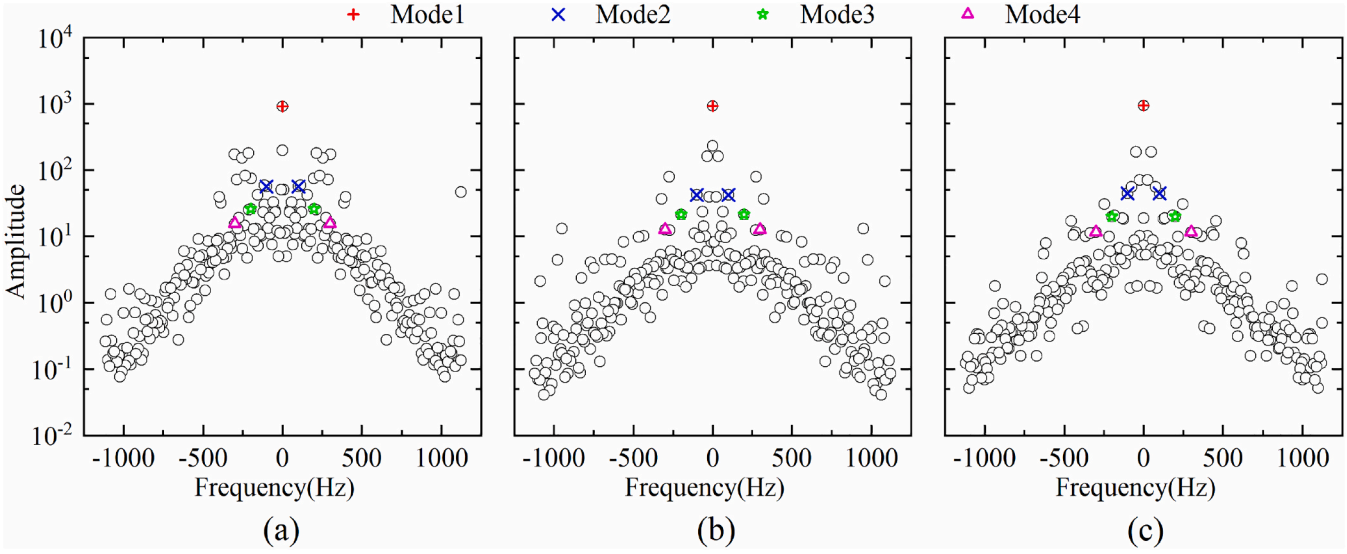

Fig. 24. Amplitude and frequency of DMD modes: (a) $x = 0.5R$, (b) $x = 2.0R$, (c) $x = 3.0R$.

part is the original flow field and the lower part is the reconstructed flow field. The reconstructed propeller wake field is in good agreement with the original propeller wake field. The propeller wake includes three parts: the tip vortex, the thin vortex sheet that sheds off from the blade trailing edge, and the hub vortex. There is an increase in the axial velocity from $x/R = 0.5$ to $x/R = 3.0$ due to the rotation of the propeller. The propeller wake changes periodically and the frequency is consistent with the blade passing frequency. Table 6 shows the reconstruction errors for three transverse planes at different instants, which are evaluated by the reconstruction error formulation in Eq. (29). The mean reconstruction errors at $x/R = 0.5$, $x/R = 2.0$, and $x/R = 3.0$ are 6.99%, 3.92%, and 3.57%, respectively, which are consistent with the errors of the first four modes in Fig. 26. The velocity at the transverse plane of $x/R = 0.5$ is greatly affected by the hub vortex, which is manifested as a larger region with small axial velocity near the hub centerline, as shown in Fig. 27.

5. Conclusions

The propeller wake dynamics under light loading conditions, such as the instability inception and transition mechanisms, have not been fully revealed or understood. The purpose of this paper is to conduct a modal analysis of the propeller wake under light loading conditions, and shed light on the coherent structures with different spatiotemporal scales, thereby laying a foundation for design optimization and flow control of the propeller. In this paper, the large eddy simulation is used to simulate the wake flow past the INSEAN E779A propeller at the advance coefficient $J = 0.85$. The vortex structures in the propeller wake are identified by the Q criterion. Dynamic mode decomposition (DMD) and reconstruction are used to analyze the wake dynamics on the central-longitudinal plane and different transverse planes. Compared with previous work, the unique contributions in this paper are: (1) DMD analysis of the propeller wake flow and a new perspective for studying the propeller wake mechanism; (2) greater understanding of propeller wake dynamics under a light loading condition through the innovative performance of dynamic mode decomposition (DMD) and

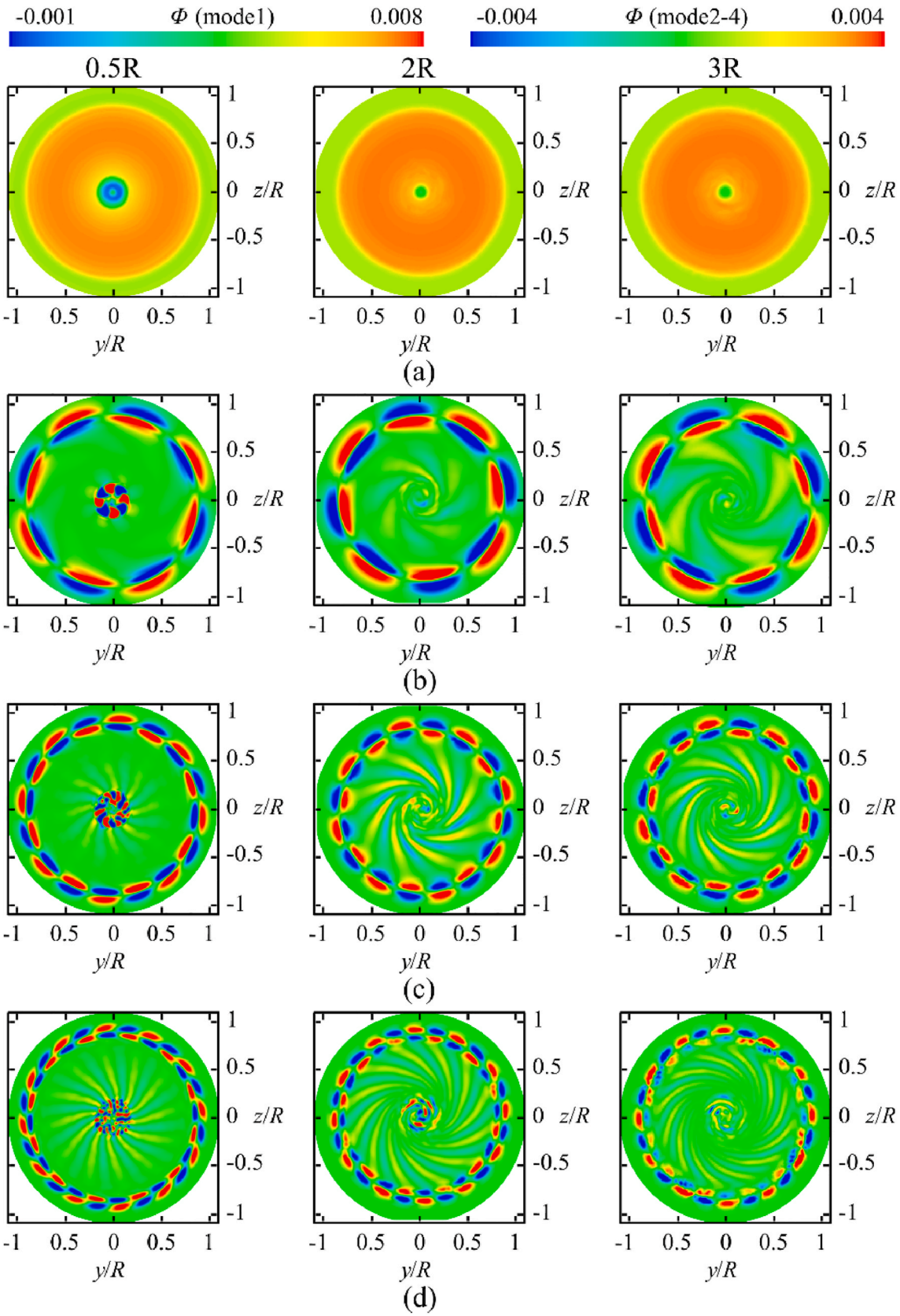

Fig. 25. The first four DMD modes of the propeller wake field: (a) mode 1, (b) mode 2, (c) mode 3, (d) mode 4, (Left: $x/R = 0.5$; middle: $x/R = 2.0$; right: $x/R = 3.0$).

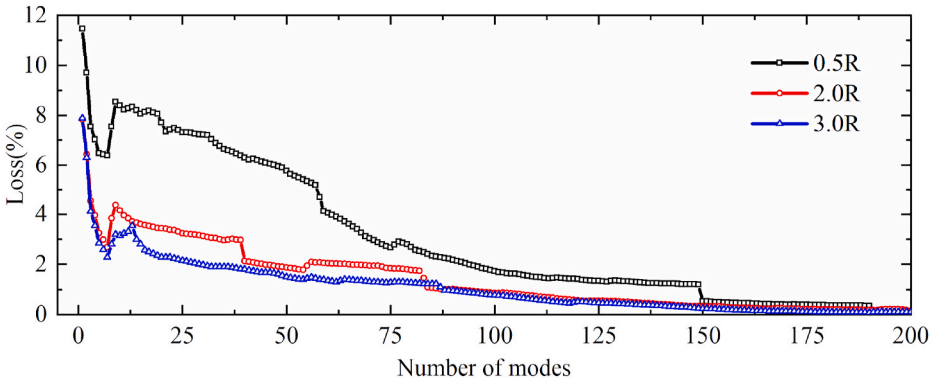

Fig. 26. The relationship between the loss function and the selected number of modes.

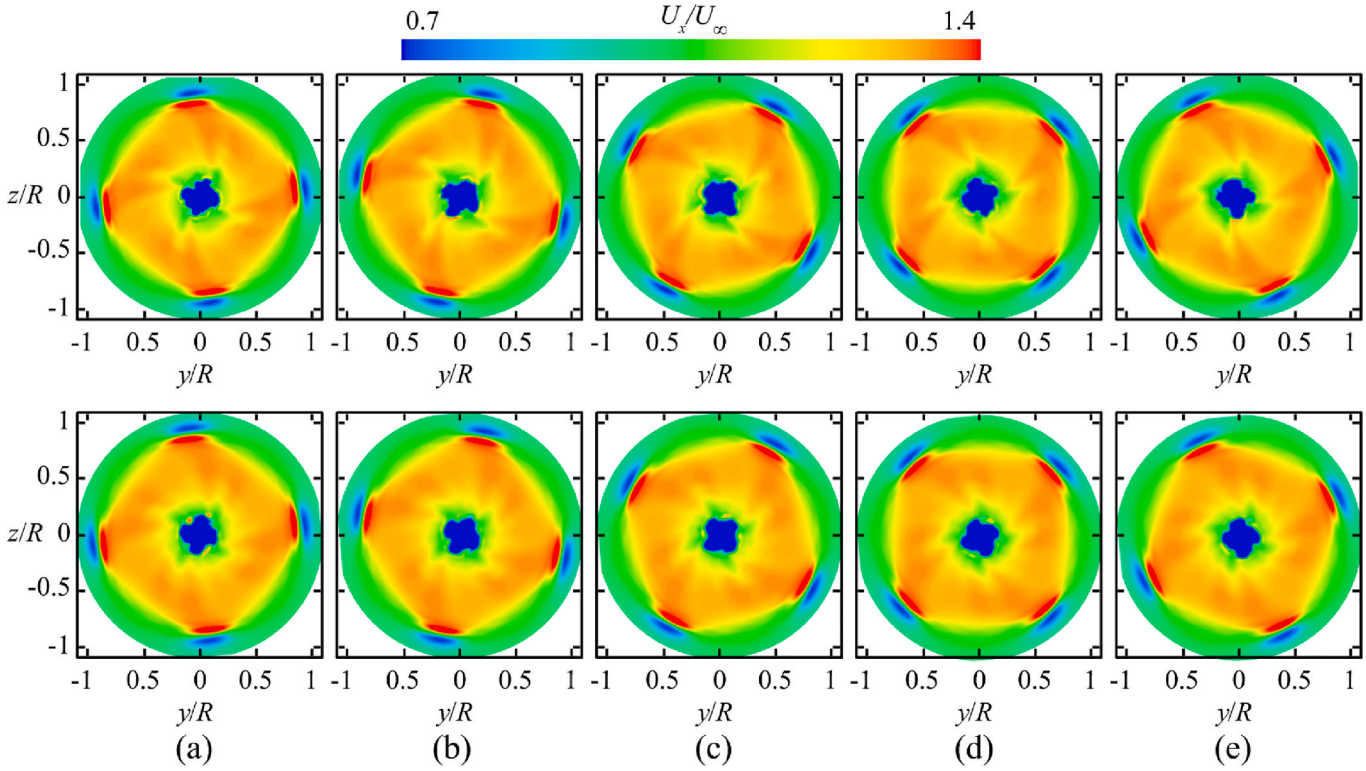

Fig. 27. The reconstructed and originally simulated axial velocity field for the transverse plane of $x/R = 0.5$ at several instants: (a) $t = 0.2$T, (b) $t = 0.4$T, (c) $t = 0.6$T, (d) $t = 0.8$T, (e) $t = 1.0$T. (Up: original flow field; bottom: reconstructed flow field).

reconstruction; and (3) development of the DMD reduced-order model to reconstruct the propeller wake with well-restored coherent structures.

Our conclusions are summarized as follows:

(1) Based on the comparisons of the performance characteristics and the wake vortex system, the present numerical approach is proven to be reliable and in good agreement with the experimental results. The propeller wake includes stable tip and hub vortices without interacting evolution, and elliptical instabilities are captured downstream of the tip vortices.

(2) DMD analysis shows that most of the eigenvalues are on the unit circle, indicating that the propeller wake is stable and periodic. Mode 1 occupies the largest proportion of total energy with 49.06% at the central-longitudinal plane, and 46.19%, 63.83%, and 65.16% at the transverse planes of $x = 0.5R$, $x = 2.0R$, and $x = 3.0R$, respectively. Both DMD and FFT can successfully obtain the dominant frequencies of the propeller wake, that is, the blade passing frequency and its multiples.

(3) DMD can identify the coherent structures of the tip and hub vortices. Mode 1 represents the mean flow field. Mode 2 depicts antisymmetric large-scale coherent structures in the tip vortex region, where modes 3-4 decompose into smaller antisymmetric turbulent coherent structures. These coherent structures are mainly related to the ordered convection of the tip vortices.

(4) DMD can reconstruct the propeller wake by using reduced-order modes. The reconstruction error gradually decreases as the selected number of modes increases. Mode 1 restores nearly 90% of the information about the propeller wake. Moreover, the reconstructed wake flow using the first four modes has a maximum error of 7.98%, and it describes the major flow features of the propeller wake, that is, the tip and hub vortex, and the thin vortex sheet shedding off from the blade trailing edge.

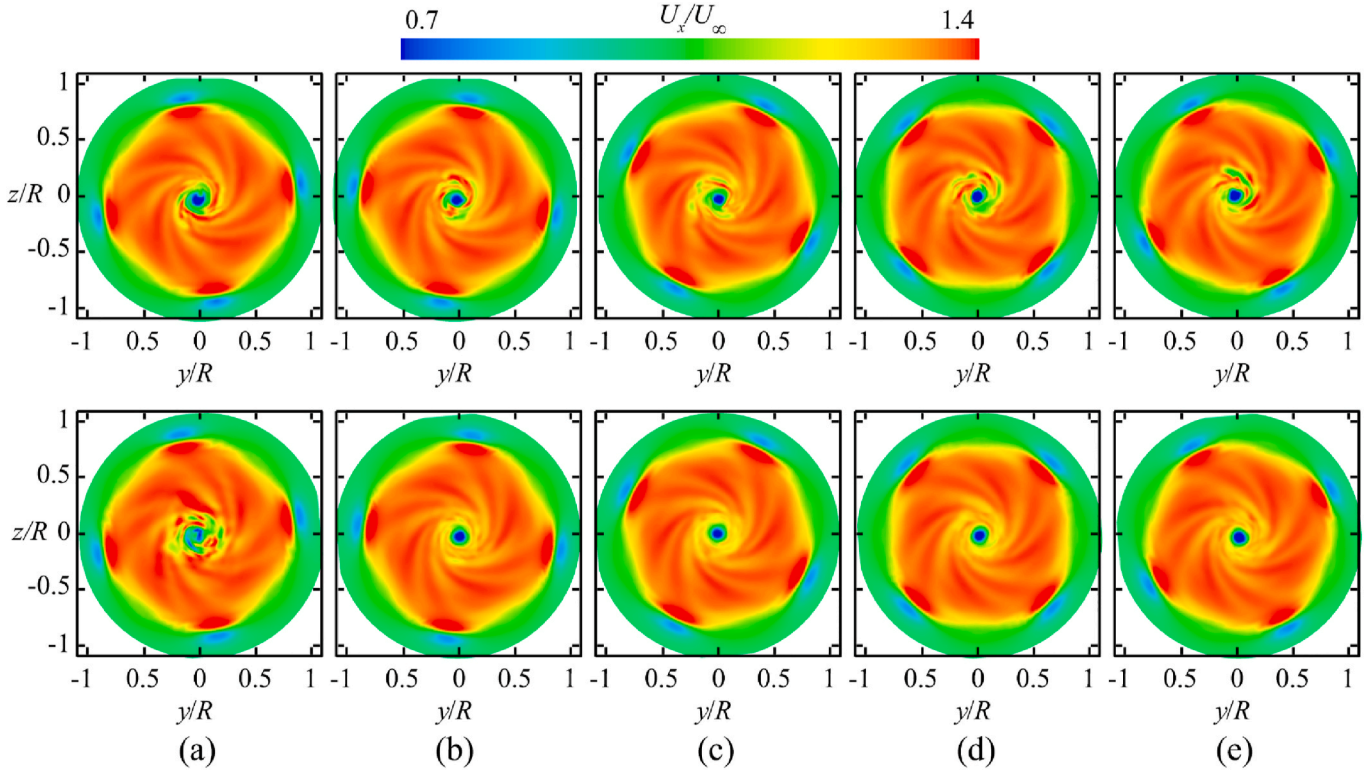

Fig. 28. The reconstructed and originally simulated axial velocity field for the transverse plane of $x/R = 2.0$ at several instants: (a) $t = 0.2$T, (b) $t = 0.4$T, (c) $t = 0.6$T, (d) $t = 0.8$T, (e) $t = 1.0$T. (Up: original flow field; bottom: reconstructed flow field).

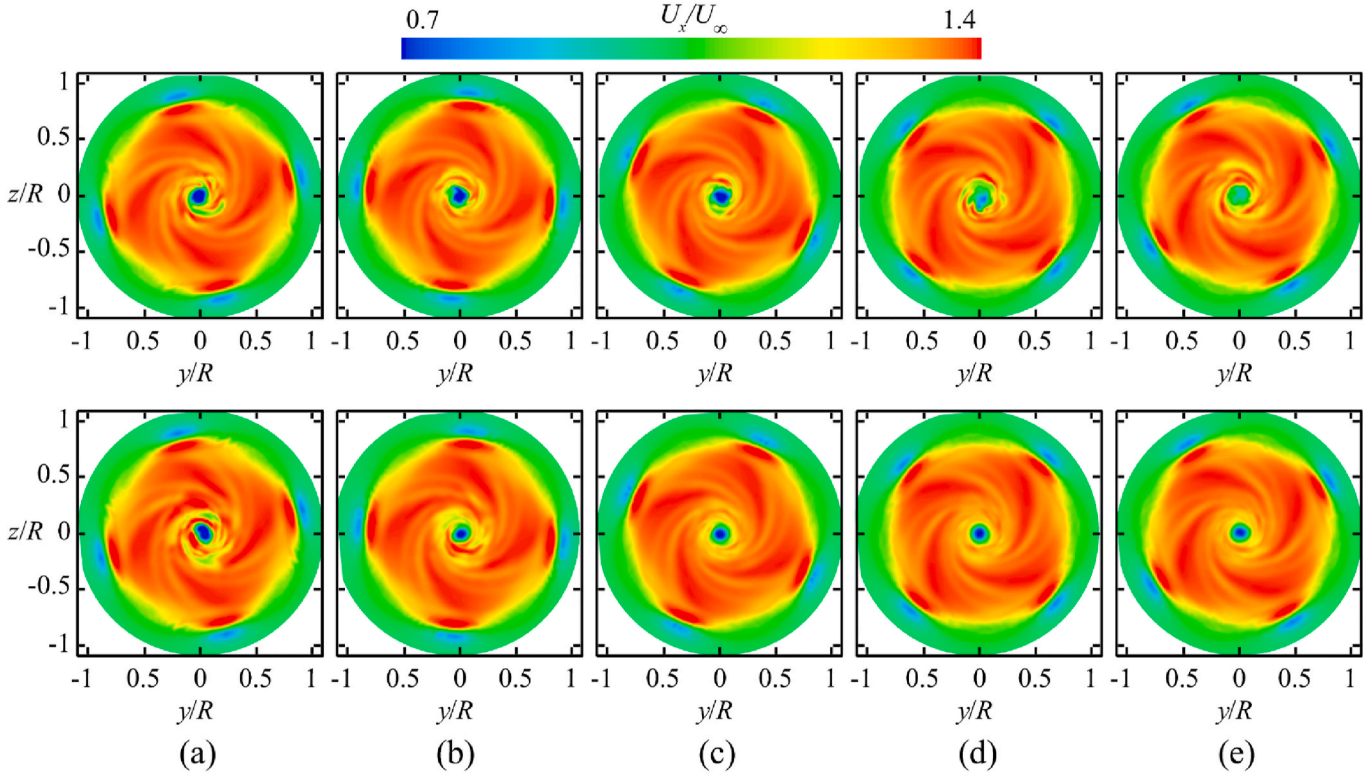

Fig. 29. The reconstructed and originally simulated axial velocity field for the transverse plane of $x/R = 3.0$ at several instants: (a) $t = 0.2$T, (b) $t = 0.4$T, (c) $t = 0.6$T, (d) $t = 0.8$T, (e) $t = 1.0$T. (Up: original flow field; bottom: reconstructed flow field).

Table 6
Reconstruction errors for three transverse planes at different instants.

	$Err_{0.20T}$ (%)	$Err_{0.40T}$ (%)	$Err_{0.60T}$ (%)	$Err_{0.80T}$ (%)	$Err_{1.00T}$ (%)	Err_{mean} (%)
0.5R	7.98	6.87	7.05	6.49	6.58	6.99
2.0R	4.21	3.85	3.69	3.81	4.03	3.92
3.0R	3.97	3.81	3.43	3.41	3.24	3.57

DMD proved to be an effective method to analyze the propeller wake dynamics. In particular, the flow-field reconstruction based on the DMD reduced-order model is useful for predicting the propeller wake and controlling the propeller operation. This work further extends our understanding of propeller wake dynamics under light loading conditions. In the future, we will further investigate DMD analysis and the reduced-order reconstruction for the propeller wake under other operating conditions.

CRediT authorship contribution statement

Yuchang Zhi: Conceptualization, Investigation, Writing – original draft. **Rundi Qiu:** Investigation. **Renfang Huang:** Conceptualization, Writing – review & editing, Supervision, Funding acquisition. **Yiwei Wang:** Funding acquisition, Supervision.

Declaration of competing interest

The authors declare that they have no known competing financial interests or personal relationships that could have appeared to influence the work reported in this paper.

Data availability

Data will be made available on request.

Acknowledgements

The authors would like to acknowledge gratefully the National Natural Science Foundation of China (No. 52006232, 12122214).

References

Ahmed, S., Croaker, P., Doolan, C.J., 2020. On the instability mechanisms of ship propeller wakes. Ocean. Eng. 213, 107609.
Bai, X., Cheng, H., Ji, B., 2022. LES Investigation of the noise characteristics of sheet and tip leakage vortex cavitating flow. Int. J. Multiphas. Flow 146, 103880.
Blanco-Rodríguez, F.J., Le Dizès, S., 2016. Elliptic instability of a curved Batchelor vortex. J. Fluid Mech. 804, 224–247.
Chase, N., Carrica, P.M., 2013. Submarine propeller computations and application to self-propulsion of DARPA Suboff. Ocean. Eng. 60, 68–80.
Chen, K.K., Tu, J.H., Rowley, C.W., 2012. Variants of dynamic mode decomposition: boundary condition, Koopman, and Fourier analyses. J. Nonlinear Sci. 22 (6), 887–915.
Cotroni, A., Di Felice, F., Romano, G., Elefante, M., 2000. Investigation of the near wake of a propeller using particle image velocimetry. Exp. Fluid 29 (1), S227–S236.
Debnath, M., Santoni, C., Leonardi, S., Iungo, G.V., 2017. Towards reduced order modelling for predicting the dynamics of coherent vorticity structures within wind turbine wakes. Phil. Trans. Math. Phys. Eng. Sci. 375 (2091), 20160108.
Di Felice, F., 2004. Experimental investigation of the propeller wake at different loading conditions by particle image velocimetry. J. Ship Res. 48 (2), 168–190.
Di Mascio, A., Muscari, R., Dubbioso, G., 2014. On the wake dynamics of a propeller operating in drift. J. Fluid Mech. 754, 263–307.
Dubbioso, G., Muscari, R., Di Mascio, A., 2013. Analysis of the performances of a marine propeller operating in oblique flow. Comput. Fluid. 75, 86–102.
Dubbioso, G., Muscari, R., Di Mascio, A., 2014. Analysis of a marine propeller operating in oblique flow. Part 2: very high incidence angles. Comput. Fluid. 92, 56–81.
Dubbioso, G., Ortolani, F., 2020. Analysis of fretting inception for marine propeller by single blade loads measurement in realistic operating conditions. Straight ahead and turning circle maneuver. Mar. Struct. 71, 102720.
Felli, M., Camussi, R., Di Felice, F., 2011. Mechanisms of evolution of the propeller wake in the transition and far fields. J. Fluid Mech. 682, 5–53.
Felli, M., Di Felice, F., Guj, G., Camussi, R., 2006. Analysis of the propeller wake evolution by pressure and velocity phase measurements. Exp. Fluid 41 (3), 441–451.
Felli, M., Falchi, M., 2018. Propeller wake evolution mechanisms in oblique flow conditions. J. Fluid Mech. 845, 520–559.
Felli, M., Felice, F.D., 2005. Propeller wake analysis in nonuniform inflow by LDV phase sampling techniques. J. Mar. Sci. Technol. 10 (4), 159–172.
Felli, M., Guj, G., Camussi, R., 2008. Effect of the number of blades on propeller wake evolution. Exp. Fluid 44 (3), 409–418.
Felli, M., Roberto, C., Guj, G., 2009. Experimental analysis of the flow field around a propeller–rudder configuration. Exp. Fluid 46 (1), 147–164.
Gong, J., Ding, J., Wang, L., 2021. Propeller–duct interaction on the wake dynamics of a ducted propeller. Phys. Fluids 33 (7), 074102.
Guo, H., Guo, C., Hu, J., Lin, J., Zhong, X., 2021. Influence of jet flow on the hydrodynamic and noise performance of propeller. Phys. Fluids 33 (6), 065123.
Han, C., Long, Y., Bai, X., Ji, B., 2021. Numerical Investigation of Unsteady Cavitation Flow Around E779A Propeller in a Nonuniform Wake with an Insight on How Cavitation Influences Vortex. Shock and Vibration 2021.
Han, Y., Tan, L., 2020. Dynamic mode decomposition and reconstruction of tip leakage vortex in a mixed flow pump as turbine at pump mode. Renew. Energy 155, 725–734.
Hattori, Y., Fukumoto, Y., 2009. Short-wavelength stability analysis of a helical vortex tube. Phys. Fluids 21 (1), 014104.
Heydari, M., Sadat-Hosseini, H., 2020. Analysis of propeller wake field and vortical structures using k− ω SST Method. Ocean. Eng. 204, 107247.
Hu, J., Zhang, W., Guo, H., Sun, S., Chen, F., Guo, C., 2021. Numerical simulation of propeller wake vortex–rudder interaction in oblique flows. Ships Offshore Struct. 16 (2), 144–155.
Jovanović, M.R., Schmid, P.J., Nichols, J.W., 2014. Sparsity-promoting dynamic mode decomposition. Phys. Fluids 26 (2), 024103.
Kao, J.-H., Lin, Y.-J., 2020. Predicting the dipole noises of the marine propeller with verifications by experimental measurements. Ocean. Eng. 209, 107451.
Kumar, P., Mahesh, K., 2017. Large eddy simulation of propeller wake instabilities. J. Fluid Mech. 814, 361–396.
Lee, S.J., 2002. Phase-averaged PTV measurements of propeller wake. In: Proceedings of the 24th Symposium on Naval Hydrodynamics, Fukuoka, pp. 18–25, 2002.
Li, H., Huang, Q., Pan, G., Dong, X., 2021. Wake instabilities of a pre-swirl stator pump-jet propulsor. Phys. Fluids 33 (8), 085119.
Liang, W., Chen, T., Wang, G., Huang, B., 2020. Investigation of unsteady liquid nitrogen cavitating flows with special emphasis on the vortex structures using mode decomposition methods. Int. J. Heat Mass Tran. 157, 119880.
Liu, M., Tan, L., Cao, S., 2020. Method of dynamic mode decomposition and reconstruction with application to a three-stage multiphase pump. Energy 208, 118343.
Liu, Y., Long, J., Wu, Q., Huang, B., Wang, G., 2021a. Data-driven modal decomposition of transient cavitating flow. Phys. Fluids 33 (11), 113316.
Liu, Y., Wu, Q., Huang, B., Zhang, H., Liang, W., Wang, G., 2021b. Decomposition of unsteady sheet/cloud cavitation dynamics in fluid-structure interaction via POD and DMD methods. Int. J. Multiphas. Flow 142, 103690.
Long, Y., Han, C., Long, X., Ji, B., Huang, H., 2021. Verification and validation of Delayed Detached Eddy Simulation for cavitating turbulent flow around a hydrofoil and a marine propeller behind the hull. Appl. Math. Model. 96, 382–401.
Magionesi, F., Dubbioso, G., Muscari, R., Di Mascio, A., 2018. Modal analysis of the wake past a marine propeller. J. Fluid Mech. 855, 469–502.
Muscari, R., Di Mascio, A., Verzicco, R., 2013. Modeling of vortex dynamics in the wake of a marine propeller. Comput. Fluid. 73, 65–79.
Nicoud, F., Ducros, F., 1999. Subgrid-scale stress modelling based on the square of the velocity gradient tensor. Flow, Turbul. Combust. 62 (3), 183–200.
Paik, B.-G., Kim, J., Park, Y.-H., Kim, K.-S., Yu, K.-K., 2007. Analysis of wake behind a rotating propeller using PIV technique in a cavitation tunnel. Ocean. Eng. 34 (3–4), 594–604.
Posa, A., Broglia, R., Balaras, E., 2020. The wake structure of a propeller operating upstream of a hydrofoil. J. Fluid Mech. 904.
Posa, A., Broglia, R., Felli, M., Falchi, M., Balaras, E., 2019. Characterization of the wake of a submarine propeller via large-eddy simulation. Comput. Fluid. 184, 138–152.
Posa, A., Felli, M., Broglia, R., 2022. Influence of an upstream hydrofoil on the acoustic signature of a propeller. Phys. Fluids 34 (4), 045112.
Qin, D., Huang, Q., Pan, G., Han, P., Luo, Y., Dong, X., 2021. Numerical simulation of vortex instabilities in the wake of a preswirl pumpjet propulsor. Phys. Fluids 33 (5), 055119.
Qiu, R., Huang, R., Wang, Y., Huang, C., 2020. Dynamic mode decomposition and reconstruction of transient cavitating flows around a Clark-Y hydrofoil. Theory Appl. Mech. Lett. 10 (5), 327–332.
Quaranta, H.U., Bolnot, H., Leweke, T., 2015. Long-wave instability of a helical vortex. J. Fluid Mech. 780, 687–716.
Quaranta, H.U., Brynjell-Rahkola, M., Leweke, T., Henningson, D.S., 2019. Local and global pairing instabilities of two interlaced helical vortices. J. Fluid Mech. 863, 927–955.
Schmid, P.J., 2010. Dynamic mode decomposition of numerical and experimental data. J. Fluid Mech. 656, 5–28.
Schmid, P.J., 2011. Application of the dynamic mode decomposition to experimental data. Exp. Fluid 50 (4), 1123–1130.
Schmid, P.J., Li, L., Juniper, M.P., Pust, O., 2011. Applications of the dynamic mode decomposition. Theor. Comput. Fluid Dynam. 25 (1), 249–259.
Shannon, C.E., 1949. Communication in the presence of noise. Proc. IRE. 37 (1), 10–21.
Shi, H., Wang, T., Zhao, M., Zhang, Q., 2022. Modal analysis of non-ducted and ducted propeller wake under axis flow. Phys. Fluids 34 (5), 055128.

Sun, C., Tian, T., Zhu, X., Hua, O., Du, Z., 2021. Investigation of the near wake of a horizontal-axis wind turbine model by dynamic mode decomposition. Energy 227, 120418.
Sun, S., Wang, C., Guo, C., Zhang, Y., Sun, C., Liu, P., 2020. Numerical study of scale effect on the wake dynamics of a propeller. Ocean. Eng. 196, 106810.
Sun, S., Zhi, Y., Li, X., Guo, Z., 2022. Numerical investigation on cavitating wake dynamic of a propeller with bionic tubercle leading-edge. Ocean. Eng. 252, 111240.
Wang, C., Li, P., Guo, C., Wang, L., Sun, S., 2022a. Numerical research on the instabilities of CLT propeller wake. Ocean. Eng. 243, 110305.
Wang, L.-Z., Guo, C.-Y., Su, Y.-M., Wu, T.-C., 2018. A numerical study on the correlation between the evolution of propeller trailing vortex wake and skew of propellers. Int. J. Nav. Archit. Ocean Eng. 10 (2), 212–224.
Wang, L., Guo, C., Wang, C., Xu, P., 2021a. Modified phase average algorithm for the wake of a propeller. Phys. Fluids 33 (3), 35146.
Wang, L., Guo, C., Xu, P., Su, Y., 2019. Analysis of the wake dynamics of a propeller operating before a rudder. Ocean. Eng. 188, 106250.
Wang, L., Liu, X., Wu, T., 2022b. Modal analysis of the propeller wake under the heavy loading condition. Phys. Fluids 34 (5), 55107.
Wang, L., Martin, J.E., Felli, M., Carrica, P.M., 2020. Experiments and CFD for the propeller wake of a generic submarine operating near the surface. Ocean. Eng. 206, 107304.
Wang, L., Wu, T., Gong, J., Yang, Y., 2021b. Numerical analysis of the wake dynamics of a propeller. Phys. Fluids 33 (9), 95120.
Wang, L., Wu, T., Gong, J., Yang, Y., 2021c. Numerical simulation of the wake instabilities of a propeller. Phys. Fluids 33 (12), 125125.
Wu, Q., Huang, B., Wang, G., Cao, S., Zhu, M., 2018. Numerical modelling of unsteady cavitation and induced noise around a marine propeller. Ocean. Eng. 160, 143–155.
Zhu, X., Sun, C., Ouyang, H., Du, Z., 2022. Numerical investigation of the effect of towers and nacelles on the near wake of a horizontal-axis wind turbine model. Energy 238, 121782.